



**Politecnico
di Torino**

Politecnico di Torino

Corso di Laurea Magistrale in Ingegneria Energetica e Nucleare

A.a. 2023/2024

Sessione di Laurea Marzo 2024

**Direct experimental comparison of YSZ
electrolytes fabrication approaches:
powder compression
and slurry casting**

Relatore:

Prof. Massimo Santarelli

Co-relatori:

Associate Prof. Martin Paidar, MSc., Ph.D.

Michal Carda, MSc., Ph.D.

Candidato:

Federico Dei Sommi

Abstract

Hydrogen related technologies have gained importance in the latest period due to the hydrogen role in the energy transition process from fossil to sustainable sources. Solid oxide cells (SOCs) represent one of the most promising technologies. Its basic unit comprises of an electrolyte, an anode and a cathode. Due to the high operation temperature (~ 800 °C) it does not need Pt-metals catalysts and features higher efficiency than lower temperature cells. However, the high operation temperature poses high requirements on the materials properties. Despite a significant material development, the electrolyte is still responsible for majority of ohmic losses in the system. An optimal electrolyte must be highly conductive and gas impermeable to achieve a high cell performance. Thus, the aim of this work of thesis is to fabricate the YSZ electrolyte with superior properties in a reproducible manner. Two different methods were used: powder compression and slurry casting, where the former is generally used for laboratory scale and the latter for industrial scale applications. The fabrication of electrolytes by powder compression was already optimized in previous works. Therefore, the properties of these electrolytes served as a reference benchmark. The main attention was, thus, paid to optimize the state-of-the-art fabrication method – the slurry casting. The morphology and electrochemical properties of fabricated electrolytes were analyzed in order to determine the impact of fabrication procedure conditions (e. g., sintering temperature and materials/slurry composition). Using both methods the electrolytes were successfully prepared. Despite a significant progress in the optimization of electrolyte preparation by slurry casting method, the gas impermeability was still compromised due to the remaining porosity within the samples. Thus, the sintering procedure needed to be optimized to ensure gas tightness. Yet,

electrolytes fabricated by slurry casting method exhibited a significantly higher ohmic resistance compared to those prepared by powder compression.

This thesis was developed in cooperation with the Department of Inorganic Technology of the University of Chemistry and Technology in Prague (UCTP), which made available its laboratories for the carrying out of the experimental process.

Contents

1. Introduction.....	7
1.1. H ₂ economy	7
1.2. Interest in SOC	8
2. Theoretical part.....	9
2.1. Structure and working principle of SOC	9
2.2. Cell design.....	11
2.2.1. Geometries.....	11
2.2.2. Supporting layer	12
2.3. State-of-the-art materials.....	13
2.3.1. Electrolyte	13
2.3.2. Fuel electrode.....	16
2.3.3. Oxygen electrode.....	16
2.4. Electrolyte fabrication methods	17
2.5. Methods	20
2.5.1. Electrochemical Impedance Spectroscopy	21
3. Aim of the work.....	24
4. Experimental part	25
4.1. Summary of used chemicals, materials, and instrumentation.....	25
4.2. Compressed powder based electrolyte	28
4.2.1. Electrolyte fabrication.....	28
4.2.2. Electrodes deposition	30

4.2.3.	Conductivity measurement	32
4.2.4.	Electrochemical characterization.....	34
4.3.	Slurry casted electrolyte.....	37
4.3.1.	Slurry preparation.....	37
4.3.2.	Electrolyte fabrication.....	39
4.3.3.	Slurry casting optimization	40
4.3.4.	Electrodes deposition	41
4.3.5.	Conductivity measurement	42
5.	Results and discussion.....	45
5.1.	Compressed powder-based electrolyte.....	45
5.1.1.	Conductivity	46
5.1.1.1.	Ag YSZ Ag sample.....	47
5.1.1.2.	LSM YSZ LSM sample.....	54
5.1.2.	Electrochemical characterization.....	61
5.2.	Slurry casted electrolyte.....	65
5.2.1.	Conductivity	81
5.3.	Comparison of compressed powder-based and slurry casted electrolyte	85
6.	Conclusions	87
7.	Bibliography.....	89
8.	Appendix	97

1. Introduction

1.1. H₂ economy

In recent years the interest in hydrogen and hydrogen related technologies has exponentially grown. Many countries have established ambitious goals in the reduction of greenhouse gases (GHG) emissions and, as such the number of sectors considering the use of low-carbon hydrogen has risen. The 2015 Paris Agreement, signed by 195 countries, is maybe the most known example of international efforts in reducing GHG emissions.

In this perspective, hydrogen has a primary role as energy vector, especially in the hard to abate sectors, where the direct use of electricity can't be the solution. This is because hydrogen can be stored, combusted, and combined in chemical and electrochemical reactions in ways that are irreplaceable by other chemicals in various technologies. Moreover, the benefits of hydrogen for energy security, local air pollution, economic development and energy access are now routinely cited [1].

There are different ways to produce hydrogen. While nowadays it is mostly produced from fossil fuels (grey and blue hydrogen) [2], under IRENA's 1.5 °C Scenario, by 2050 hydrogen demand reaches 613 Mt (74 EJ), at least two-thirds of which should be produced from electrolysis using renewable electricity (green hydrogen) [3].

Solid oxide cell (SOC) represents a promising technology for the production of green hydrogen, particularly in large scale, stationary applications. Therefore, it can play an important role in the ambitious energy transition process and in the fight against climate change.

1.2. Interest in SOC

There is an increasing interest in hydrogen related technologies nowadays, for many reasons.

The solid oxide fuel cell (SOFC) is the most efficient type of fuel cell involved with hydrogen and hydrocarbon based fuels, especially when it works with combined heat and power (CHP). Its importance originates from being a conversion tool from chemical to electrical for generation of power without noise, pollution, and can be safely handled [4]. Other positive aspects of the SOFCs are the high energy efficiency, the high power density that could be achieved, the scalability and the flexibility of using different fuels like hydrocarbons, natural gas, ammonia, biogas, hydrogen, and even municipal wastes [5], [6], [7].

On the other hand, a combination of solid oxide electrolysis cells (SOECs) and power from renewable energy is an efficient pathway for the production of hydrogen and syngas, with several advantages: SOECs are able to efficiently use the intermittent energy resources as an input for electrolyzing process and are also able to reduce the emissions of carbon dioxide to the atmosphere by recycling (or re-using) and converting it to syngas [8], [9].

The solid oxide cell technology also presents some issues. The operation with steep chemical potential gradient, as well as temperature gradient, leads to severe requirements for materials stability and compatibility. Therefore, the material selection and a proper fabrication procedure of the different components of the cell become crucial [10]. The problem of degradation is more significant in electrolysis than in fuel cell operation, posing even more attention on the material requirements [11], [12].

2. Theoretical part

2.1. Structure and working principle of SOC

A Solid Oxide Cell is an electrochemical cell, i.e., a device driving a complete Red-Ox reaction with separated oxidation and reduction half-reactions. Its basic unit comprises of:

- An electrolyte, where the ions are conducted while molecules and electrons cannot pass through
- An anode, where the oxidation reaction occurs
- A cathode, where the reduction reaction occurs

SOCs can be operated in fuel cell mode, during which electricity from hydrogen or other energy resources such as hydrocarbons, CO, etc. is being produced. On the other hand, SOC's can be operated in electrolysis mode, during which hydrogen (or syngas) and oxygen is being produced from H₂O (and CO₂) when the electricity is supplied [13], [14].

The working principle of a SOC operating in fuel cell mode or in electrolysis mode is shown in Figure 1 and Figure 2 respectively. For clarity and conciseness, only the cases with hydrogen and water as fuels are reported here.

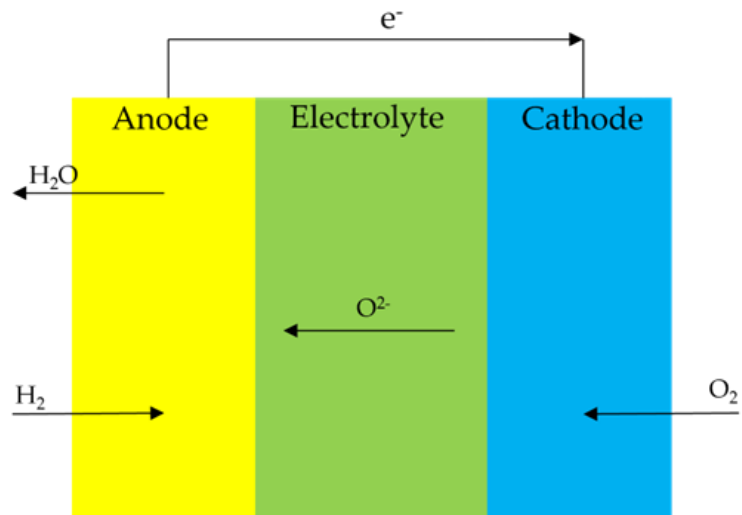


Figure 1 - A schematic of a SOFC using H_2 as fuel

The reactions occurring are the following:

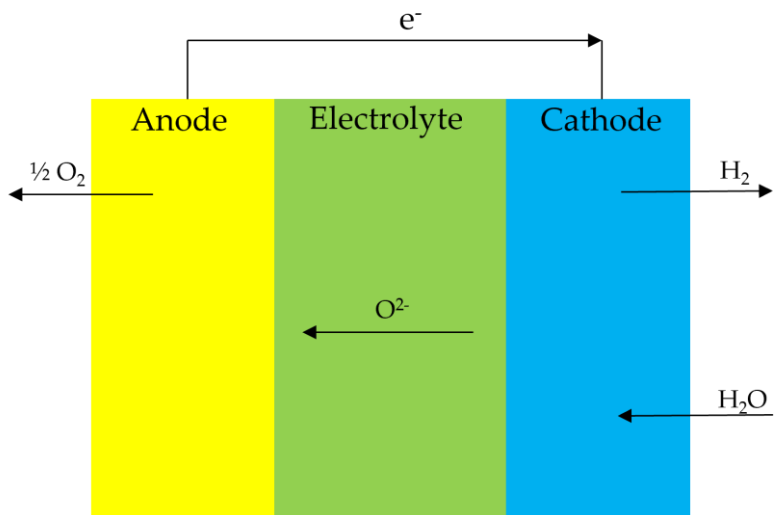
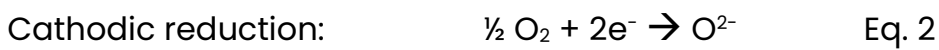
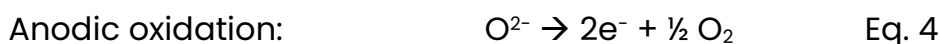


Figure 2 - A schematic of a SOEC producing H_2 from water

The reactions occurring are the following:



2.2. Cell design

2.2.1. Geometries

Although various possibilities are present, the tubular and the planar geometries are the most popular for solid oxide cells [15], and they are shown in Figure 3.

The most significant advantage of tubular configuration is that it does not require any sealing [16], which represents one of the challenging elements in these systems. On the other hand, the planar configuration requires hermetic seals to prevent fuel and oxidant mixing but features higher efficiency and power density [17]. Moreover, planar cells are generally characterized by simple construction, cheap fabrication and ease of integration but their configuration leads to a very high demand for the thermal stability of the materials, reducing the lifetime of the system. In contrast, tubular cells can elevate tolerance to long-term thermal cycling, effectively shorten startup time, realize higher volumetric output density and portable characteristics [18].

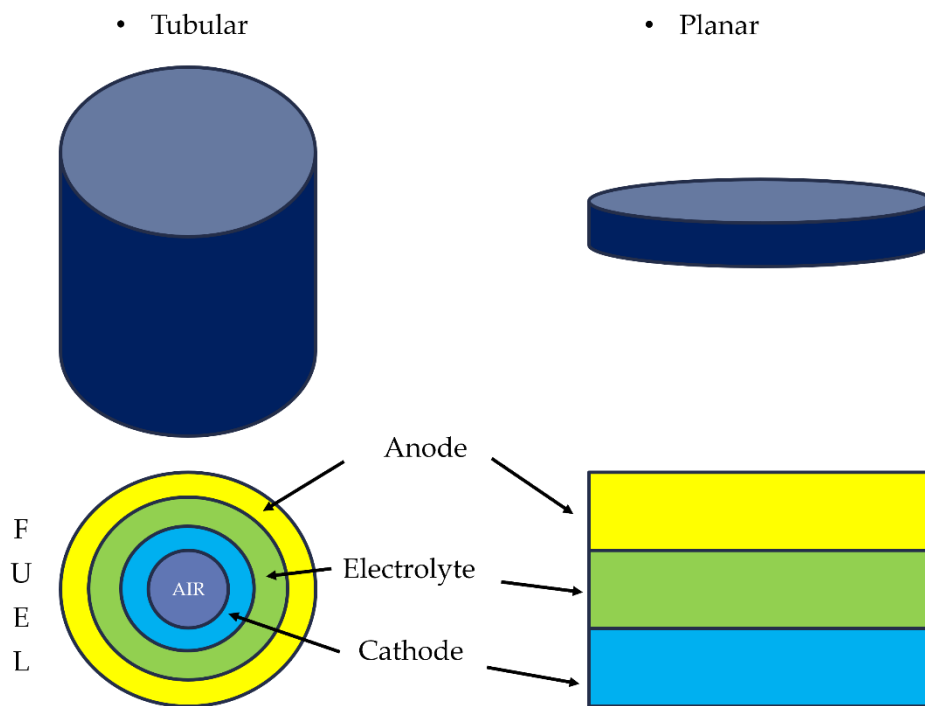


Figure 3 - Schematic of tubular and planar SOCs

2.2.2. Supporting layer

The supporting layer is a crucial component of each cell as it is directly responsible for its overall mechanical integrity. Generally, four different types of cell designs are used, namely: cathode supported cell, electrolyte supported cell (ESC), anode supported cell (ASC) and externally supported cell, shown in Figure 4. The cell component that gives the name to the design is the thickest one to provide the mechanical support to the entire cell. The electrode supported cells (anode and cathode supported cells) feature higher performance with respect to the electrolyte supported ones, due to the thinner electrolyte (its thickness can be reduced from 40÷300 μm of the ESC to less than 20 μm of the electrode supported cell). In contrast, ESCs are more robust and less susceptible to mechanical failures. ASCs represent the state-of-the-art of the electrode supported design and, together with the ESC, is the dominating design used in SOCs development and applications. The externally supported cells are not so

widespread yet, presenting the main issue of increasing the complexity of the structure [19], [20], [21]. Despite this slight disadvantage, the metal-supported cells are currently intensively developed for applications with large area cells.

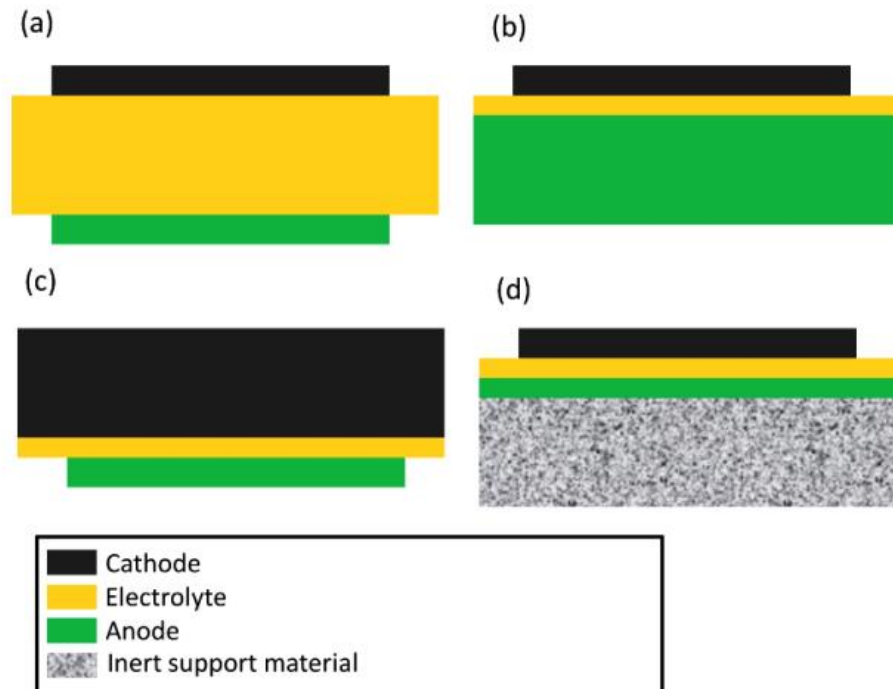


Figure 4 - Different types of cell designs: (a) electrolyte; (b) anode; (c) cathode; (d) externally supported [20]

2.3. State-of-the-art materials

2.3.1. Electrolyte

The materials for the components of a solid oxide cell are generally based on various ceramic materials exhibiting the properties required for the individual cell components.

The electrolyte should feature a very high ionic conductivity and a low (preferably none) electronic conductivity, gas tightness, a proper mechanical strength, a good thermo-chemical stability and should be cost-effective. The most widely used material is Yttria-stabilized zirconia (YSZ), i.e., ZrO_2 doped with Y_2O_3 . The most

common Y_2O_3 dopant concentration is the 8 mol% of yttria (8YSZ), as this composition exhibits the highest conductivity [22]. Among other possible materials is Scandia-stabilized zirconia (ScSZ) i.e., Sc_2O_3 doped with ZrO_2 . It shows a significantly higher conductivity and better chemical stability compared to YSZ. The major issues in the utilization of this material are the availability and price of Scandia [23], [24], [25]. Both materials, i.e. YSZ and ScSZ, are examples of oxide-ion conductive materials, which is preferred for high temperature operation ($>700\text{ }^\circ\text{C}$).

Other materials have been developed and investigated as electrolytes for intermediate temperature cells. They can be oxide-ion conductive, such as Ceria-doped materials and doped lanthanum silicate apatites, but also proton conductive, such as BaCe- and BaZr-based oxides while Lanthanum tungstates are a promising proton conductive candidate for high temperature operation [26]. Ceria-based electrolyte materials, such as samarium-doped ceria (SDC) or gadolinium-doped ceria, exhibit the highest ionic conductivity at operating temperatures between $400\text{ }^\circ\text{C}$ and $800\text{ }^\circ\text{C}$ [27]. Also, the perovskite material LaGaO_3 , that produces $\text{La}_{1-x}\text{Sr}_x\text{Ga}_{1-y}\text{Mg}_y\text{O}_3$ (LSGM) if doped with Sr and Mn, presents good O^{2-} conductivity at low temperatures [23]. Although, the intermediate operating temperature would be preferred due to lower material requirements and significantly retarded rate of degradation, the above mentioned materials usually exhibit a rather high electron conductivity. Such property is undesirable for electrolytes as it allows for shunt currents, and thus, effectively reducing the Faradaic efficiency of the process.

Table 1 summarizes the main advantages and disadvantages of YSZ, ScSZ, Gd doped Ceria and LSGM candidate materials [28].

YSZ	Gd doped CeO₂	LSGM	ScSZ
<p>↑ Excellent stability in oxidizing and reducing environment</p> <p>↑ Excellent mechanical stability (especially 3YSZ)</p> <p>↑ >40 000 h of fuel cell operation possible</p> <p>↑ High quality raw materials available</p> <p>↓ Low ionic conductivity (especially 3YSZ)</p> <p>↓ Incompatible with some cathode materials</p>	<p>↑ Good compatibility with cathode materials</p> <p>↑ Mixed electronic-ionic conductor at low pO₂ (application in anode cermets)</p> <p>↓ Electronic conduction at low pO₂ → low OCV</p> <p>↓ Mechanical stability</p> <p>↓ Availability and price of Gd</p>	<p>↑ Good compatibility with cathode materials</p> <p>↓ Phase stability</p> <p>↓ Ga evaporation at low pO₂</p> <p>↓ Incompatible with NiO</p> <p>↓ Mechanical stability</p> <p>↓ Availability and price of Ga</p>	<p>↑ Excellent stability in oxidizing and reducing environment</p> <p>↑ Possible better long-term stability than 8YSZ</p> <p>↓ Availability and price of Sc</p>

Table 1 - Advantages and disadvantages of possible electrolyte materials [28]

2.3.2. Fuel electrode

The electrodes should be active in electrochemical reactions, good ionic and electrical conductors, they should be porous to allow sufficient mass transfer, they should be thermo-chemically stable during the cell operation, and finally they should be compatible with the electrolyte layer.

The most common material for the fuel electrode is a Ni-8YSZ composite, with 40% volume of Ni and 60% of 8YSZ [29]. It may present some limitations, such as Sulphur poisoning and Carbon deposition [30]. Therefore, alternative materials are under research and development, such as cubic fluorite structures, perovskite-related structures, and others [31].

2.3.3. Oxygen electrode

Concerning the oxygen electrode, the state-of-the-art are perovskites (La,Sr)(Co,Fe)O₃-based materials (LSCF) and La_{0.8}Sr_{0.2}MnO_{3-δ}-based materials (LSM) with optimized microstructures. LSCF is a mixed ionic and electronic conductive (MIEC) material that presents a high electrical and ionic conductivity and high oxygen diffusion properties (oxygen diffusion and oxygen surface exchange coefficients), achieving superior electrocatalytic activity. LSM is considered as a reference material thanks to its chemical and thermal stabilities in addition to acceptable performance [22]. To improve ionic conductivity and electrochemical activity, oxygen electrodes with alkaline earth metal ions as dopants of the perovskite structure are a possible option, even though the tendency for enrichment and segregation of these elements to surfaces and interfaces often result in degradation in performance, which can be further exacerbated by the presence of other contaminants such as chromium from

interconnect materials, boron from sealants, as well as carbon dioxide, water vapor, and other minor contaminants from ambient air [32].

2.4. Electrolyte fabrication methods

Several methods have been proposed and researched for the fabrication of solid oxide cells electrolytes.

Uniaxial powder compression and slurry casting are preferentially selected to form a solid electrolyte from powder precursors. Uniaxial compression is a fast and inexpensive molding method for the preparation of pellets of any shape. However, its drawback is its limited applicability, mainly for laboratory research purposes, because it produces relatively thick ($>500 \mu\text{m}$) pellets. On the other hand, the slurry casting method allows electrolytes to be produced approximately $100 \mu\text{m}$ thick, or even thinner. However, this method is more complicated and expensive compared to uniaxial compression [33], mainly because of the need for additives.

In the powder compression, the electrolyte is simply prepared by pressing a certain amount of powder in a steel mold, obtaining the so-called green body, and then sintering [34], [35].

In the tape casting, the powder is mixed with selected additives to obtain a solution (the slurry) with desired rheological properties. A list of possible additives with their function is available in Table 2. The additives marked with an asterisk are typically employed in the aqueous tape casting, where a water-based slurry replaces the more common organic solvent-based one. With respect to organic solvent-based solutions, in the water-based solutions non-toxic and non-flammable additives are used, but they are more difficult to handle and very sensitive to process variations [36].

Name	Function
Polyvinyl Butyral (PVB)	Binder
Hydrolyzed polyvinyl alcohol*	Binder
Ethanol	Solvent
Toluene	Solvent
De-ionized water*	Solvent
Diethyl-o-phthalate (DEP)	Plasticizer
Benzyl butyl phthalate	Plasticizer
Polyethylene Glycol (PEG)	Plasticizer
Glycerol*	Plasticizer
Triton	Dispersant
Poly-acrylic acid*	Dispersant
Ammonia*	Electrostatic dispersant
1-octanol*	De-foamer
Secondary alcohol ethoxylate	De-foamer
2,4,7,9-tetramethyl-5-decyne-4,7-diol ethoxylate*	Surfactant
Starch powder*	Pore former
Carbon black*	Pore former
Graphite flakes*	Pore former

* typically used in aqueous tape casting

Table 2 - List of possible additives to be employed in the tape casting [36], [37], [38], [39], [40], [41]

The fabricated slurry, organic- or water-based, is casted by a machine called doctor blade, i.e., a device with adjustable height of slit allowing for spreading

viscous materials with uniform height, then dried, and finally sintered [42], [43]. A schematic of the slurry casting procedure is shown in Figure 5.

Reducing the thickness of the electrolyte to 5 - 10 μm is possible with this technique, however it cannot provide the mechanical support of the cell anymore.

Examples of state-of-the-art processing methods used in industrial scale or well-established in lab scale besides powder compression and slurry casting for the fabrication of electrolytes are screen printing, where a prepared suspension is placed on the screen and is forced by pressure for its passage and electrophoretic deposition (EPD), where an electric field is applied forcing charged particles suspended in a liquid to move toward an electrode with opposite charge. Other methods, such as thermal spraying, extrusion, wet powder spraying, sol-gel, physical vapor deposition (PVD), chemical vapor position (CVD), pulsed-laser deposition (PLD), electrospray deposition (ESD) are possible but not very popular [20], [21].

In this work, powder compression and slurry casting methods were considered, as the aim was to fabricate electrolyte supported cells (ESCs) in a simple and lab-scale manner.

The sintering represents an important step in the fabrication process. The way how the sintering is carried out can influence important properties of the electrolyte, such as its porosity, its surface roughness, its morphology in general and, as a consequence, its electrochemical and mechanical properties. The optimal sintering process can vary according to the materials and procedure employed to fabricate the green body, thus it results important to analyze this aspect case by case [44], [45].

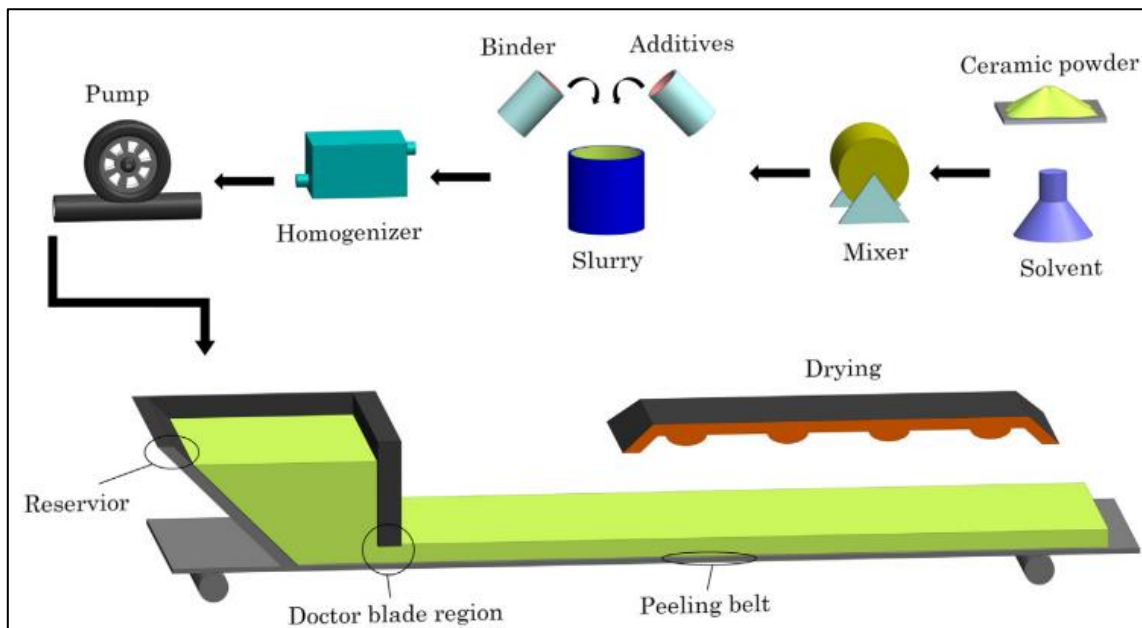


Figure 5 - Tape casting procedure [43]

2.5. Methods

The majority of characterization methods used within the experimental part of this thesis are standard in the field of electrochemical characterization (e.g., cyclic voltammetry, open circuit measurement) or in the field of morphological material analysis (e.g., SEM, optical microscopy). As such, these standard techniques will not be discussed within this thesis as the relevant information is easily accessible. For example, further information can be found in *"ELECTROCHEMICAL METHODS: Fundamentals and Applications"* [46]. Nevertheless, the application of electrochemical impedance spectroscopy for SOC may pose a challenge to the correct evaluation of data, therefore a short overview of such method is given.

2.5.1. Electrochemical Impedance Spectroscopy

Electrochemical impedance spectroscopy (EIS) is a very useful tool for solid oxide cells analysis.

Electrochemical impedance measurements are realized in a whole frequency range, typically from kHz to mHz, and typically shown in a Nyquist plot or a Bode plot. By varying experimental parameters such as applied potential, temperature, reactant composition, etc. frequency shifts in the impedance spectra can be observed, revealing information on electrochemical processes governing the system. Besides, one strong characteristic of this method is that measurements can be done while the system is functioning i.e. in-situ measurements, allowing access to information that would not be obtained otherwise (with post-mortem characterization methods for instance). Such feature is even more significant for SOC examination as the range of in-situ methods is limited due to the high operation temperature. However, the interpretation of impedance spectra can quickly become challenging, requiring the use of additional tools such as electrical equivalent circuit (EEC), distribution of relaxation time (DRT) or analysis of the difference in impedance spectra (ADIS) for a better and deeper understanding [47].

The common approach of fitting the impedance spectra with equivalent electrical circuit models is sufficient for overall performance comparison. The EEC are combination of ideal (resistor, capacitor, inductor, etc.) and non-ideal (constant phase element or CPE, Warburg, etc.) electrical elements in series and/or in parallel [47], [48], [49].

The EIS is generally plotted in Nyquist plot, which is a graph where the real part (Z') of the impedance is on the x axis and the imaginary part (Z'') of the impedance is on y axis. Figure 6 represents one of the EIS spectra acquired during

a measurement of the conductivity of a SOFC electrolyte, now taken as an example. Z' indicates the real part and Z'' the imaginary part of the impedance, in Ohm. The abscissa of the intersection point with the x axis represents the ohmic resistance of the measured system. This value can be obtained fitting the curve by an equivalent circuit.

An example of equivalent circuit is shown in Figure 7, the so-called Randles circuit. Every component describes some properties or events happening in the system under study:

- The inductor $L1$ describes the interference to the acquisition due to the surroundings, such as the supply wires, the furnace and etc.
- The resistor $R1$ represents the ohmic resistance of the electrolyte
- The two couples of resistor and condenser in parallel ($R2-CPE1$ and $R3-CPE2$) represent the reactions occurring at each electrode

The point related to the ohmic resistance always corresponds to high frequency values. This is because the electron transfer step is usually considered as the fastest step (compared to electrode reaction, etc.).

The equivalent circuit is not unique but may change from curve to curve. This happens because, differently from a liquid means, the behavior of a solid oxide cell (and in general of a solid means) is neither easily predictable nor always smooth and simple, yielding to the necessity to adapt any time the fitting to the observed situation.

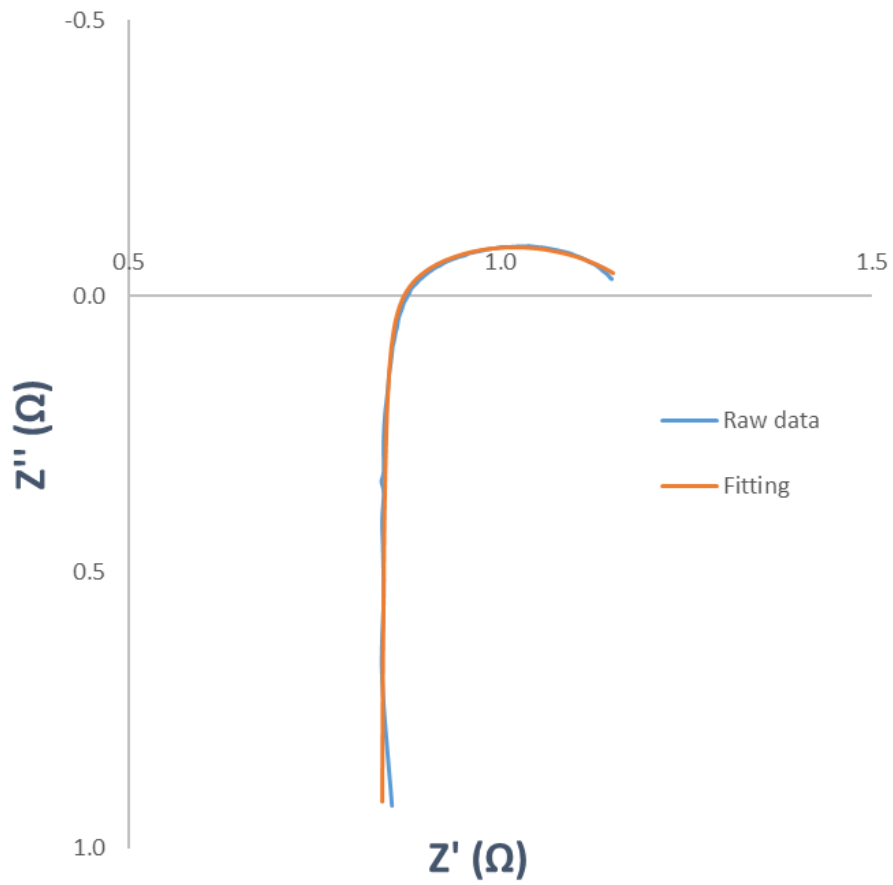


Figure 6 - Example of EIS spectrum with the corresponding fitting curve

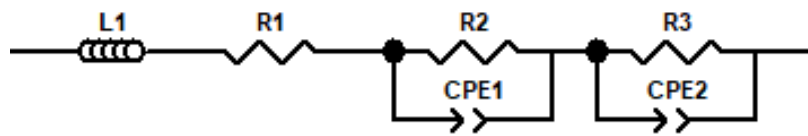


Figure 7 - Most complete equivalent circuit for the fitting of the EIS spectra

3. Aim of the work

Solid oxide cells are considered a very promising technology to promote the transition of the current energy scenario towards more sustainable sources. The operation at high temperature and chemical potential of SOCs poses a big challenge in the development and fabrication of suitable materials, able to withstand such an adverse environment. Despite the several studies, this aspect is still an open task, presenting broad space for further research in the topic. This thesis aims at exploring two approaches for the fabrication of YSZ electrolytes: powder compression and slurry casting.

These approaches should be employed to fabricate electrolytes whose shape, morphology and electrochemical properties will be investigated. Where required, the fabrication procedure should be optimized by trying several alternatives and evaluating the effects on the final product.

4. Experimental part

4.1. Summary of used chemicals, materials, and instrumentation

- List of chemicals and materials

Trademark® (IUPAC name)	Purity/Composition	Supplier
α -terpineol (2-(4-methylcyclohex-3-en-1-yl)propan-2-ol)	$\geq 96\%$, per analysis	Merck Life Science s.r.o.
Ethanol	Denatured ethanol, 5% methanol	BIOFERM - lihovar Kolín, a.s.
Ethylene glycol (ethane-1,2-diol)	99%, per analysis	PENTA s.r.o.
Toluene G.R.	C_7H_8	Lach-Ner s.r.o.
TERGITOL	Type 15-S-9	Merck Life Science s.r.o.
Diethyl Phthalate	$\geq 99\%$, per analysis	Merck Life Science s.r.o.
LSM20-P	$(La_{0.80}Sr_{0.20})_{0.95}MnO_{3-\delta}$	fuelcellmaterials, a Nexceris company
TZ-8YS	$(Y_2O_3)_{0.08}(ZrO_2)_{0.92}$	Tosoh Corporation
TZ-8YSB	$(Y_2O_3)_{0.08}(ZrO_2)_{0.92} + 3$ wt.% $CH_3[CH_2]_{16}COOH$	Tosoh Corporation
YSZ8-TC	$(Y_2O_3)_{0.08}(ZrO_2)_{0.92}$	fuelcellmaterials, a Nexceris company
Ag ₂ O	-	UCT lab preparation
Ag mesh	-	Safina, a.s.

Au wires	99.99%	Safina, a.s.
Alumina (Luxal) sheets/tubes	Al ₂ O ₃	ESTCOM CZ, oxidová keramika a.s.
O ₂	99.5%	SIAD Czech s.r.o.
N ₂	99.999%	SIAD Czech s.r.o.

Table 3 - List of employed chemicals and materials

– List of instruments

Instrument type	Trademark®	Supplier	Country of origin
Analytical scales	ARJ 220-4M	Kern & Sohn	Germany
External furnace regulator	Clare 4.0	Clasic CZ s.r.o.	Czech Republic
Frequency response analyzer	SI 1250	Ametek/Solartron Metrology	United Kingdom
Electrochemical interface (potentiostat)	SI 1287	Ametek/Solartron Metrology	United Kingdom
High temperature furnace with regulator	Laboratory elevator furnace	Clasic CZ s.r.o.	Czech Republic
Hydraulic press	H-62	Trystom s.r.o.	Czech Republic
Infrared IC heater	T-962 DGC	PUHUI T DGC SHZ	China
Laboratory furnace	Small cylindrical furnace	Clasic CZ s.r.o.	Czech Republic

Optical Microscope	Axio Scope A1	Carl Zeiss Microscopy Deutschland GmbH	Germany
Programmable LCR bridge	HM8118	Rohde&Schwarz GmbH (HAMEG Instruments)	Germany
Scanning electron microscope	S-4700/EDAX	Hitachi, Ltd.	Japan
Screen-printing station	VARIANT A5	M. Špalek - STZ Choltice	Czech Republic
Ultrasound bath	DT 255 H	BANDELIN electronic GmbH & Co. KG	Germany
Vacuum dryer suitable for magnetic stirrer	-	FisherScientific	Czech Republic
Ultrasound generator (+ horn)	GM 3100 (VS70/T)	BANDELIN electronic GmbH & Co. KG	Germany
Tape caster	CNCTape caster	CZ Robotics	Czech Republic
Membrane vacuum pump	Laboport N838	KNF Group	Germany
Mass flow meter/controller	EL-FLOW Select	Bronkhorst High-Tech B.V.	The Netherlands
Doctor blade	-	-	-

Table 4 - List of employed instruments

4.2. Compressed powder based electrolyte

In this chapter will be described the first investigated YSZ electrolyte fabrication approach: the powder compression.

In the specific, it will be described how the compressed powder based electrolyte was fabricated, how its conductivity was measured and how the electrochemical properties of a complete cell were characterized. An optimization of the fabrication process was not necessary as it had been already optimized by the work of the research group at UCTP, summarized in an article by Carda et al. [33]. In both the fabrication approaches, YSZ was employed as material for the electrolyte. This choice was mainly due to its availability, its current widespread utilization for this purpose and to the experience about YSZ gained by the research group at UCTP.

4.2.1. Electrolyte fabrication

To fabricate the electrolyte, 3 g of YSZ powder (TZ-8 YSB) by Tosoh (Figure 8) were uniaxially compressed in a hydraulic press H-62. The powder was first inserted in a metallic mold of 3.6 cm in diameter, to give the electrolytes a circular shape. Filtration paper sheets were placed between the mold and the powder, to prevent the degradation of the former and the adhesion of powder to the mold. The press, together with the mold and the sheets, are shown in Figure 9.



Figure 8 - YSZ powder by Tosoh Corporation



Figure 9 - Hydraulic press, mold, and paper sheets

The operation of compression resulted in a disk of compressed YSZ powder (Figure 10), called green body. The green body was sintered at 1360 °C for 6 hours (for the complete sintering procedure look at sintering protocol 1 in Appendix table I) in a high temperature furnace (laboratory elevator furnace), obtaining finally the electrolyte of approximately 0.9 mm in thickness and 2.8 mm in diameter (Figure 11).



Figure 10 - Green body



Figure 11 - Compressed powder based electrolyte

4.2.2. Electrodes deposition

Once the compressed powder based electrolyte was produced, it was necessary to deposit electrodes on it, to make possible the conductivity measurement and the electrochemical characterization. Two different types of electrode inks were fabricated and then deposited. One was based on LSM and made up by mixing 2 g of LSM20-P powder with 1.0 mL of terpineol (Figure 12), while the other was based on Ag_2O and was made up by mixing 3 g of Ag_2O powder and 2.1 mL of ethylene glycol (Figure 14).

The electrodes were deposited by two different methods, according to the type of paste:

- Screen printing for LSM ink → the paste was deposited using the screen-printing station VARIANT A5 (Figure 13)
- Brush deposition for Ag_2O ink → the paste was deposited simply by using a brush



Figure 12 - LSM paste



Figure 13 - Screen printing station



Figure 14 - Ag₂O paste

Symmetrical cells were fabricated, meaning that electrodes of the same material were deposited on both sides of the electrolyte, obtaining two-electrode (counter and working electrode) and three-electrode (counter, working and reference electrode) assemblies.

After the deposition, the deposited electrodes were dried in an Infrared IC heater, before being sintered in a high temperature furnace (laboratory elevator furnace). The Ag electrodes were sintered at 800 °C for 2 hours (sintering protocol 3 of Appendix table I) while the LSM electrodes were sintered at 1150 °C for 3 hours (sintering protocol 4 of Appendix table I). The cells after the sintering are shown in Figure 15, Figure 16 and in Figure 17. The two-electrode assembly cells were employed for the conductivity measurement while the three-electrode assembly cell was employed for the electrochemical characterization.

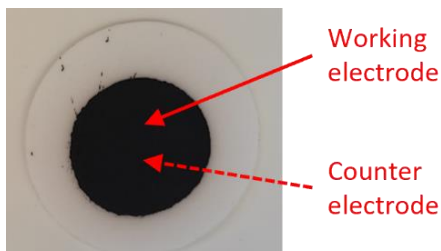


Figure 15 - Two-electrode cell with LSM electrodes, compressed powder

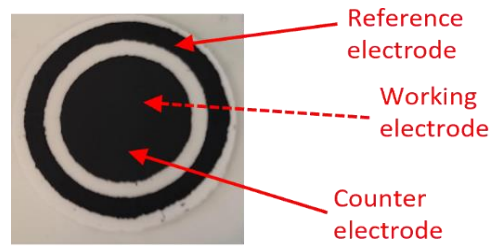


Figure 16 - Three-electrode cell with LSM electrodes, compressed powder

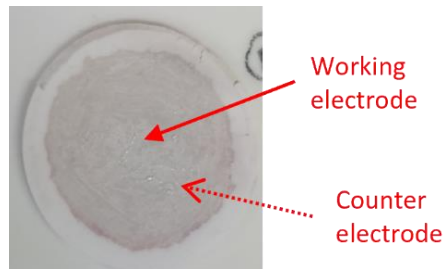


Figure 17 - Two-electrode cell with silver electrodes, compressed powder

4.2.3. Conductivity measurement

Electrochemical impedance spectroscopy was utilized to determine the compressed powder-based electrolyte conductivity. The experimental apparatus for the acquisition of the impedance spectra was composed of the laboratory furnace (small cylindrical furnace), the external furnace regulator Clare 4.0 and the Programmable LCR bridge HM8118. The electrodes of the cell were linked to the LCR bridge through two silver wires, each of them joined to a silver mesh, working as current collector. To achieve a good electrical contact, a grid of Ag ink was drawn onto the electrodes, before connecting them to the silver mesh and wires. An example of mesh drawing is represented in Figure 19. The cell was then inserted between two alumina boats that were tightened using Ti wires, to keep the electrical contact during the experiment (Figure 18). The atmosphere inside the furnace was controlled thanks to a gas feed with controlled flow meters

and the whole setup was located in a quartz tube to ensure stabilized atmosphere conditions during the experiments.

This apparatus was used both for LSM and silver electrodes samples.

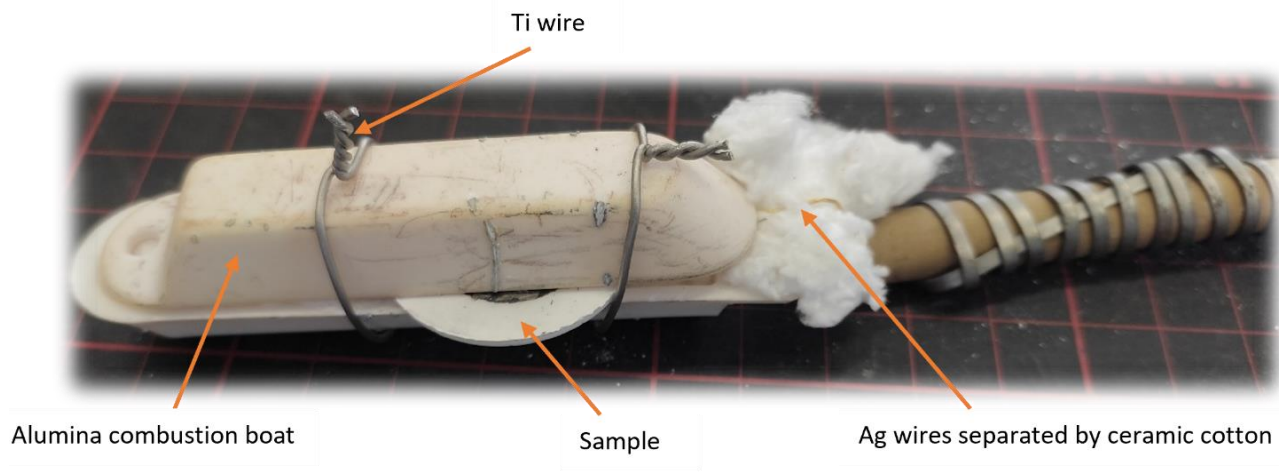


Figure 18 - Sample ready for the conductivity measurement

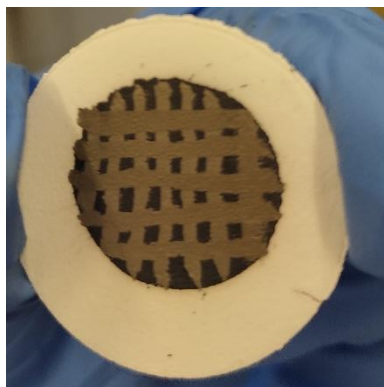


Figure 19 - Ag mesh drawn on LSM electrode

The experimental conditions used for Ag and LSM samples are summarized in Table 5.

	Ag	LSM
Temperature [°C]	400, 450, 500, 550, 575, 600, 625, 650, 700, 750, 800	400, 450, 500, 550, 575, 600, 625, 650, 700, 750, 800
Gas composition	100% O ₂ 100% N ₂	100% O ₂ 100% N ₂
Voltage	Open circuit voltage	Open circuit voltage
Amplitude	50 mV	50 mV
Frequency	200 kHz to 20 Hz	200 kHz to 20 Hz

Table 5 - Experimental conditions for conductivity measurement, Ag and LSM samples of compressed powder based electrolyte

Once the value of ohmic resistance was obtained from the fitting of the EIS spectra, the last step was to calculate the conductivity. It was done according to Eq. 7:

$$\sigma = \frac{t}{A \cdot R} \quad \left[\frac{S}{m} \right] \quad \text{Eq. 7}$$

where

- σ is the conductivity [S/m]
- t is the thickness of the electrolyte [m]
- A is the area of one electrode (the two electrodes occupy the same area) [m²]
- R is the ohmic resistance of the electrolyte [Ω]

4.2.4. Electrochemical characterization

The experimental apparatus was composed of two housing parts, located vertically against each other. Individual parts, i.e. half-cell housings, allow to accommodate current collectors, seal, and the sample itself. The sample housing

is divided by the sample itself to two different sections: one included the reference (RE) and counter electrode (CE) and the other included the working electrode (WE). Two mica papers were added to reduce the gas permeability from one section to the other. As such, different gas compositions could be fed into the individual electrode compartments. The electrodes were connected to a frequency response analyzer through supply wires. The electrical connections were obtained in the same way as described in the conductivity measurement paragraph, with the only difference regarding the RE that was connected directly with the wire, without using a mesh, but only adding Ag ink in the point of contact. The frequency response analyzer was connected to an electrochemical interface. The apparatus was then inserted into a laboratory furnace, to be able to reach the high operational temperatures typical of solid oxide cells. The experimental apparatus is represented in Figure 20.

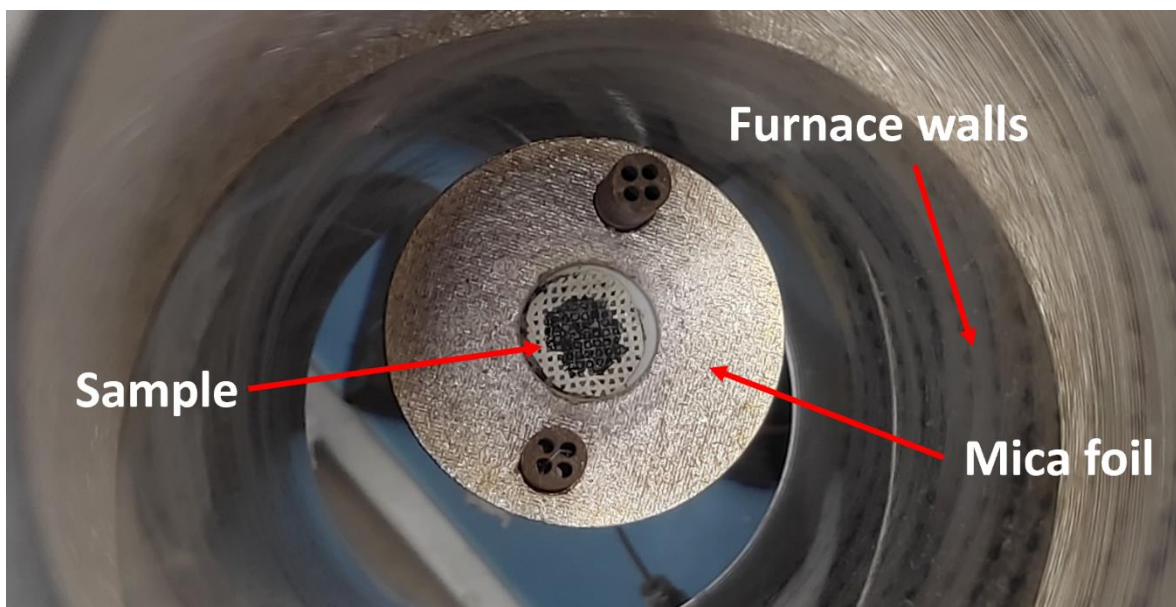


Figure 20 - One section of the experimental apparatus for the electrochemical characterization of a complete cell, seen from above

Three temperature levels were analyzed: 800, 700 and 600 °C. The gas mixture at RE and CE was kept constant at 100% O₂ for the whole measurement to ensure the stable potential of RE, while at WE it was varied between 100% and 20% O₂ at each temperature. The potentiostatic, potentiodynamic and EIS methods were employed to characterize the cell. While the potentiodynamic method of cyclic voltammetry was used only to make the cell more active, the characterization was actually based on the potentiostatic and the EIS methods, namely: open circuit measurement, chronoamperometry at stationary potential, EIS. Open circuit measurements were done for 10 minutes, chronoamperometry measurements were performed for 5 minutes at each corresponding potential. The potential range was <-0.7, 0.7> V vs RE, with each individual potential spaced by 0.1 V and measured separately. For the EIS, the parameters were used the same as in Table 5.

The measurement resulted in the values of current related to each potential. The specific current *j* was then obtained dividing the current by the area of the electrodes and the value of the ohmic resistance was obtained from the EIS.

At this point, the overpotential (η) could be calculated, according to Eq. 8:

$$\eta = V - OCP - R_{corr} \cdot I \quad [V] \quad \text{Eq. 8}$$

where

- V is the potential [V]
- OCP is the open circuit voltage of the cell [V]
- R_{corr} is the ohmic resistance multiplied by a correction factor equal to 0.9 [Ω]
- I is the current [A]

4.3. Slurry casted electrolyte

In this chapter will be described the second investigated YSZ electrolyte fabrication approach: the slurry casting.

In the specific, it will be described how the electrolyte was produced, the conductivity measured and how the optimization of the fabrication process was carried out.

4.3.1. Slurry preparation

TZ-8YS powder was mixed with selected additives (see Table 6) to obtain a solution, called slurry (Figure 21).



Figure 21 - The slurry

The first slurry solution produced, now on called base composition, resulted from the modification of one suggested by the PVB supplier, (i.e., Kuraray). The base composition, with the function of its individual constituents, is shown in Table 6.

Name	Role	Quantity	Binder solution
Toluene	Solvent	7.6 mL = 6.3 g	
Ethanol	Solvent	2.25 mL = 1.63 g	
Mowital® B60 HH	PVB binder	1.4 g	
Tergitol™	Anti-foamer	3 drops	
Diethyl phthalate	Plasticizer	0.59 mL = 0.59 g	
TZ-8YS	YSZ powder	15 g	

Table 6 – Base composition slurry

The base composition is in the weight ratio of 60% ceramic powder vs 40% binder solution.

The slurry was produced mixing the compounds in a glass container in the following order:

1. Ethanol
2. Diethyl phthalate
3. Tergitol™
4. Toluene
5. PVB
6. YSZ powder

Once the solution was completed, it underwent a 30 minutes ultrasound bath to be homogenized and to remove eventual air bubbles entrapped inside. At this point the solution was ready to be casted.

4.3.2. Electrolyte fabrication

The slurry was spread on a glass using a doctor blade (Figure 23), thus obtaining a tape (Figure 22). The thickness of the freshly casted tape has a major impact on the mechanical properties of the electrolytes after the sintering procedure. Thus, the presented work includes a parametric study of this influence as the doctor blade allows to adjust the slit height at micrometric scale.



Figure 22 - Casted tape



Figure 23 - Doctor blade

Due to its high volatility, Toluene tended to evaporate from the tape. To slow down this evaporation and avoid the formation of cracks, the fabricated tape was covered by a Petri dish. After the evaporation stopped (from 30 to 90 minutes waiting time – longer time was necessary for thicker tapes), the tape was dry enough to be detached from the glass, using a knife (Figure 24). Afterwards, it was cut to obtain stripes to be sintered in a furnace. Finally, after sintering in a high temperature furnace with regulator, a solid self-supporting electrolyte was obtained (Figure 25).



Figure 24 - Slurry casted electrolyte tape detached from the glass support



Figure 25 - Slurry casted electrolytes

A recap of the steps followed in the slurry casted electrolyte fabrication is given by Figure 26.

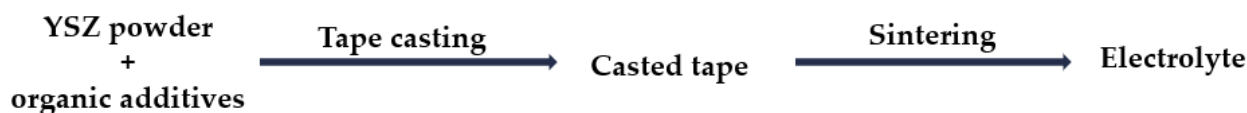


Figure 26 - Main steps in the fabrication of slurry casted electrolyte

4.3.3. Slurry casting optimization

The optimization of the slurry casting method was performed by adjusting various physical properties of the slurry, e.g., viscosity or solvent:ceramic powder ratio. Individual steps in the procedure were carried out in various modifications, comparing the resulting solid electrolyte with reference sample. The reference was decided to be the procedure carried out with the base composition slurry (Table 6), applying 1360 °C/6 hours sintering (selected as an optimal temperature for electrolyte fabrication based on powder compression) and 500 μm slit height. The variations in the fabrication procedure interested the YSZ powder and PVB binder content in the slurry, the sintering temperature and time

and the slit height. The details will be illustrated in the Results and discussion section.

The effects of the variations on the electrolyte were evaluated by means of optical or scanning electron microscopy.

4.3.4. Electrodes deposition

Once the electrolyte was produced, the electrodes were deposited to permit the conductivity measurement. For time reasons, it was not possible to perform the electrochemical characterization of the slurry casted electrolyte cell.

Two electrodes were deposited by brush deposition, both using the same Ag_2O ink of the compressed powder based electrolyte, resulting in a symmetrical 2-electrode assembly.

After the deposition the cell was dried for 5 minutes at 100 °C in an Infrared IC heater T-962 DGC and then sintered at 800 °C for 2 hours (sintering protocol 3 of Appendix table I). The final product is shown in Figure 27.

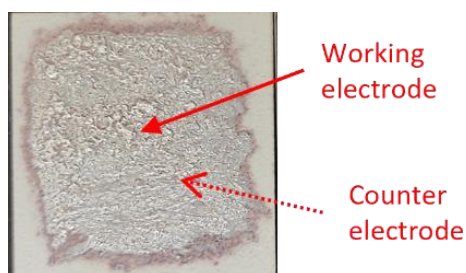
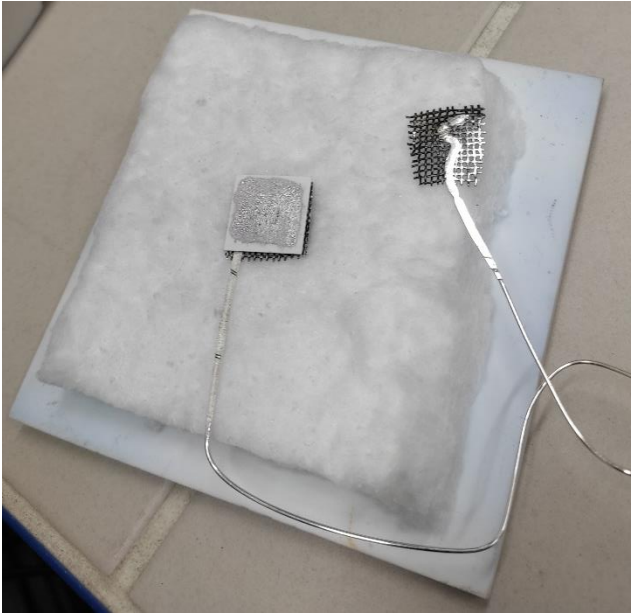


Figure 27 - Two-electrode assembly with Ag electrodes, slurry casting

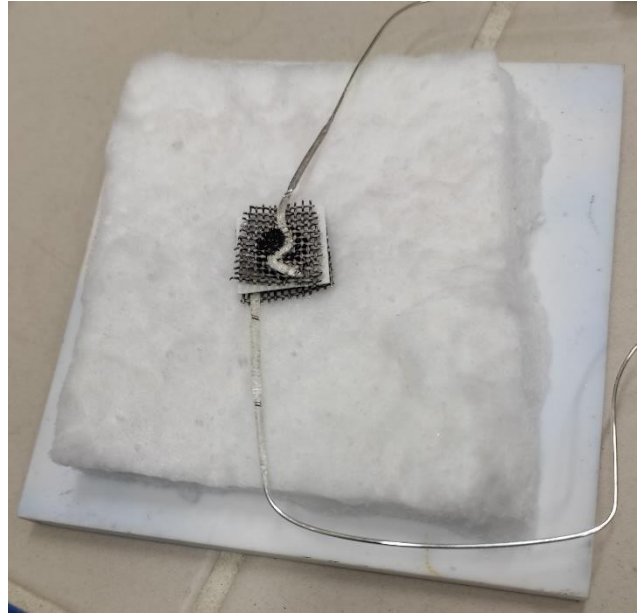
In this case, the shape of the cell is a square. This is possible thanks to the procedure of slurry casting, where a large tape is casted and then can be cut in desired shapes and dimensions, differently from the powder compression where the constraint of the mold is present.

4.3.5. Conductivity measurement

EIS was applied to determine the slurry casted electrolyte conductivity. The experimental apparatus was analogous to the one employed for the compressed powder based electrolyte, with small differences due to the thinner and more fragile mechanical properties of slurry casted electrolyte. It was composed of the laboratory furnace (small cylindrical furnace), the external furnace regulator Clare 4.0 and the Programmable LCR bridge HM8118. The electrodes were linked to the LCR bridge by means of silver wires. The wires were joined to a silver mesh, working as current collector. It wasn't possible to squeeze the sample inside the alumina boats because it would break, due to its limited mechanical integrity. Therefore, to ensure a good electrical contact, it was placed between two foils of ceramic fiber and then, gently, covered by two alumina plates. Moreover, the mesh drawn on the electrodes was replaced by a big drop of fresh Ag_2O ink between the electrodes and the current collector. Some sequences of the sample preparation procedure are shown in Figure 28.



(a)



(b)



(c)

Figure 28 - Slurry casted sample preparation for conductivity measurement: (a) the sample on one foil of ceramic fiber and alumina plate, with one bare electrode and one silver mesh ready to be placed; (b) the sample on one foil of ceramic fiber and alumina plate, with the electrode covered by the silver mesh and the fresh ink; (c) the sample placed between two foils of ceramic fiber, ready to be covered by a second alumina plate and go into the furnace

To save time, the measurement was taken only with air inside the furnace, since the same experiment with the compressed powder based electrolyte confirmed the independence of the conductivity on the gas composition (see Results and discussion part for experimental validation of such claim). The temperature was varied from 400 to 800 °C. All the experimental conditions employed are summarized in Table 7.

Temperature [°C]	Gas composition	Voltage	Amplitude	Frequency
400, 450, 500, 550, 575, 600, 625, 650, 700, 750, 800	Air	Open circuit voltage	50 mV	200 kHz to 20 Hz

Table 7 - Experimental conditions for conductivity measurement, slurry casted electrolyte

Once the value of ohmic resistance was obtained by fitting the EIS spectra, the conductivity was calculated according to Eq. 7.

5. Results and discussion

5.1. Compressed powder-based electrolyte

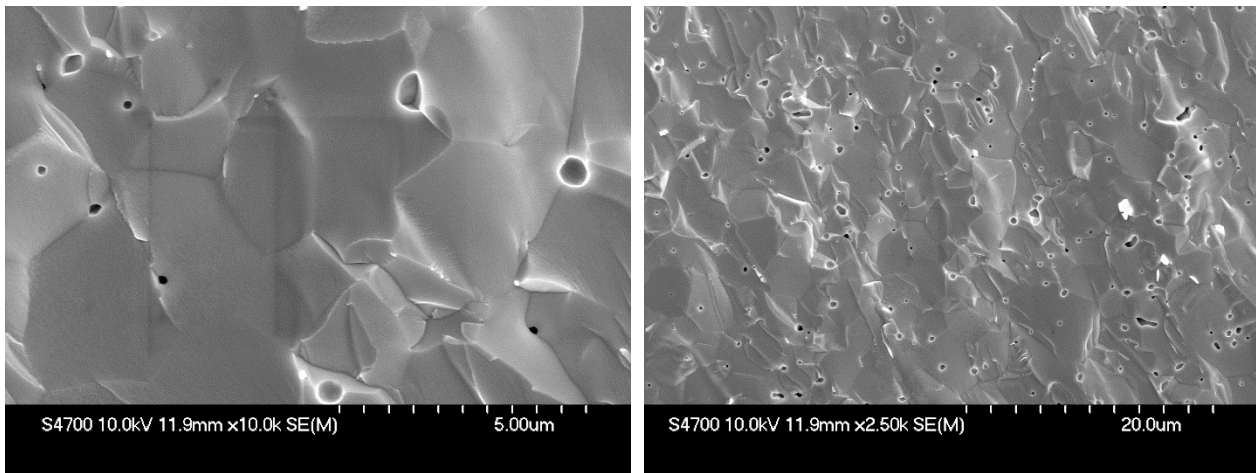
The compressed powder-based electrolytes were successfully fabricated. The resulting electrolytes were about 1 mm thick and 20 mm in diameter. Their color was white and their surface was cleaned of any leftover filtration paper by means of a ceramic knife. The morphology, phase composition and porosity were examined by means of SEM, XRD and mercury porosimetry, respectively. Finally, its conductivity and electrochemical properties were also characterized.

Above-mentioned structural and morphological analyses were carried out in specialized UCT laboratories. All analyses were performed on the sintered electrolyte, without any electrode deposition.

The XRD resulted in a pure YSZ cubic phase, as was expected. This test was executed just to confirm that the high temperature sintering did not affect the chemistry of the compound.

The porosity resulted approximately 4.95%. As the mercury porosimetry can evaluate only porosity of open pores, it can be concluded that this value of porosity is consistent with the gas tightness required by a SOC electrolyte.

The morphology was investigated solely at the sample cross-section. The pictures acquired are shown in Figure 29. Despite a net of minor defects is apparent from the images, the electrolyte is dense and tight with homogeneous well-interlinked structure.



(a)

(b)

Figure 29 - SEM images, at different magnifications, of a compressed powder based electrolyte: (a) 400x; (b) 100x

5.1.1. Conductivity

The measurement of conductivity was performed on two symmetrical samples, yet with different electrodes' materials as described in Experimental section, i.e., LSM and Ag. The gas atmosphere in which the samples were placed was varied, repeating the experiment with 100% O₂ and 100% N₂. The aim was to verify if the different type of electrodes or the different atmosphere could affect the electrolyte conductivity.

EIS spectra were acquired for each temperature level considered. For the purpose of this thesis, the only point of interest is the intersection of the curve with the x axis, since its abscissa represents the ohmic resistance of the electrolyte. The spectra were fitted employing a Randles circuit. Generally, the reactions at the electrodes form two arcs (one for each electrode) on the EIS but in certain cases only one arc is visible, making possible a simplification in the equivalent circuit. This happens when one arc is too small, or the two arcs are overlapping, and it is not possible to distinguish them with equivalent circuit fitting. Such an event

usually occurs when there is a symmetrical cell and high temperature operation. Going at lower temperatures the behavior of the system is more complicated and the two arcs may be distinguishable. Therefore, the EEC was varied according to the curve that had to be fitted, starting from the most complex version presented in the Theoretical part, Figure 7, and eventually eliminating one or more components when some simplifications were possible.

The visualization of the EIS from raw experimental data, the implementation of the equivalent circuits and the fitting results were achieved using the software ZView® by Scribner, LLC.

The ohmic resistance obtained is that of the whole measured system (electrolyte, electrodes, current collectors, wires), yet the resistance of electrodes, current collectors and wires is negligible with respect to that of the electrolyte, the obtained resistance value can be used directly as electrolyte itself. The ohmic resistance was used to calculate the electrolyte conductivity, using Eq. 7. The thickness of the electrolyte was measured by means of a caliper, while the electrode area was measured using optical analysis by means of ImageJ freeware analysis software. The next paragraphs will present the results of the measurement in the different conditions analyzed, which complete set can be found in Table 5 of the experimental part.

5.1.1.1. Ag|YSZ|Ag sample

For the Ag|YSZ|Ag sample the electrolyte resulted 1.065 mm thick and the electrode area 3.24 cm² wide.

- 100% N₂ atmosphere

The EIS spectra for the N₂ atmosphere are shown in Figure 30. It can be immediately noticed that with increasing temperature the total impedance

response decreases. Moreover, after a certain threshold, around 600 °C, the reduced impedance is more evident. For this reason, the spectra at higher temperatures are not well distinguishable from the chart, and this is why an enlargement of the 800 °C impedance curve is represented in Figure 31, taken as representative of that region.

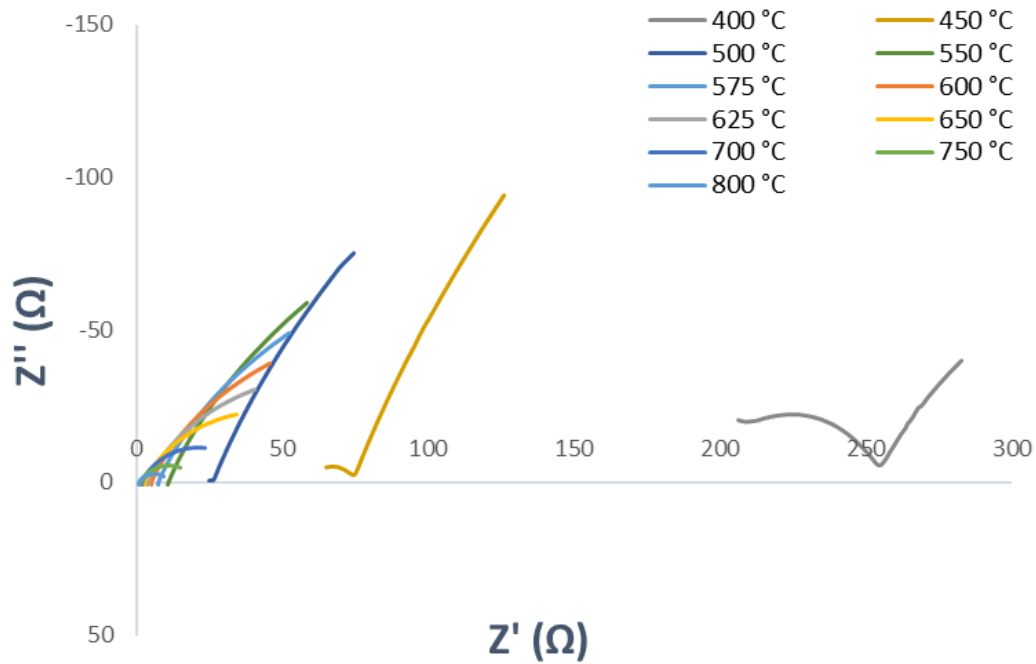


Figure 30 - EIS spectra, Ag-YSZ-Ag sample, 100% N₂

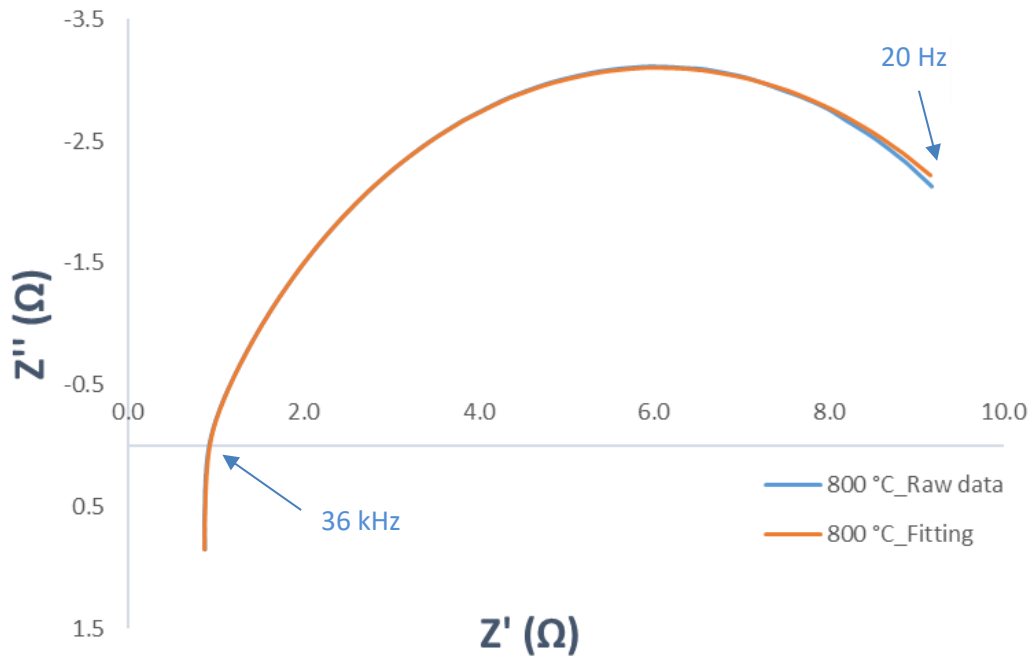


Figure 31 - EIS spectrum, Ag-YSZ-Ag sample, 800 °C and 100% N_2

Comparing the 800 °C spectrum with the ones at lower temperature, visible in Figure 30, can also be noticed that the behavior of the data becomes well-ordered and easily analyzed with high accuracy.

The values of ohmic resistance and conductivity of the electrolyte for each temperature, obtained from the impedance data elaboration, are reported in Table 8.

Temperature [°C]	Ohmic resistance [Ω]	Conductivity [S/m]
400	251	0.0131
450	73.6	0.0448
500	26.0	0.127
550	10.7	0.307
575	7.23	0.455
600	5.05	0.652
625	3.66	0.900
650	2.73	1.21
700	1.63	2.02
750	1.11	2.96
800	0.841	3.91

Table 8 - Ohmic resistance and conductivity of the electrolyte, Ag-YSZ-Ag sample, 100% N₂

From the results is evident that at higher temperature the conductivity results higher, confirming the needing of keeping a high operational temperature for such a device. At relatively low temperatures the conductivity becomes really very low, suggesting that this type of devices should not be operated at low temperatures, as it was expected. The natural logarithm of the conductivity was plotted against the reciprocal temperature, to produce the Arrhenius plot in Figure 32. It can be seen that the conductivity follows the Arrhenius trend, with some disturb at the highest temperatures. This is the effect of the wires from the experimental setup and does not compromise at all what was just deduced.

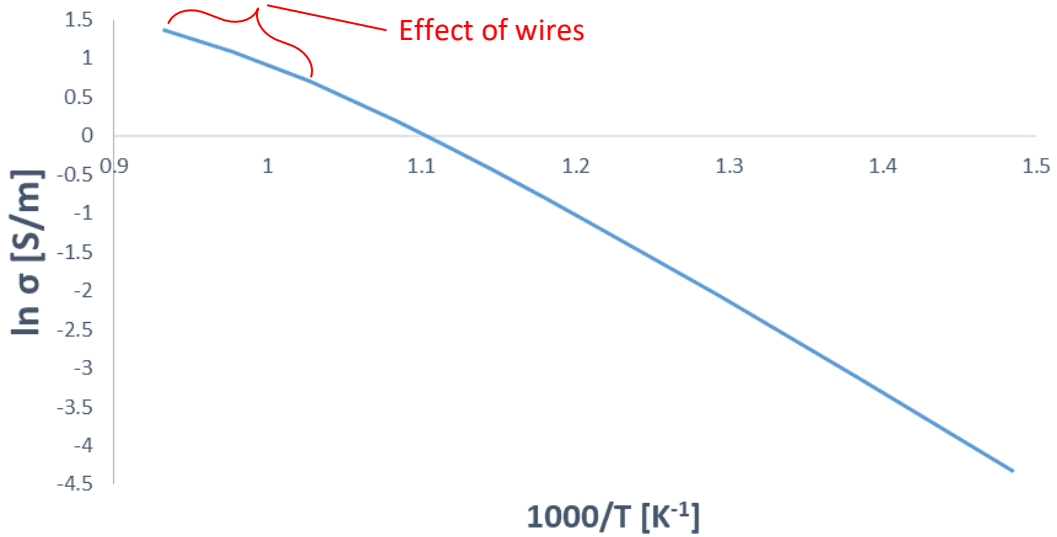


Figure 32 - Arrhenius plot, Ag-YSZ-Ag sample and 100 % N₂

- 100% O₂ atmosphere

For time reasons, the experiment with 100% O₂ atmosphere has been held at fewer temperature levels, only 5: 800, 750, 700, 650 and 600 °C.

The EIS spectra are shown in Figure 33. Again, with increasing temperature the total impedance response decreases. In this case, having excluded the lower temperatures from the experiment, the spectra result less distant from each other and the behavior of the sample remains orderly for the whole range, with the acquisition of well-ordered spectra, as a result. Nevertheless, an enlargement of the 800 °C spectrum is available in Figure 34.

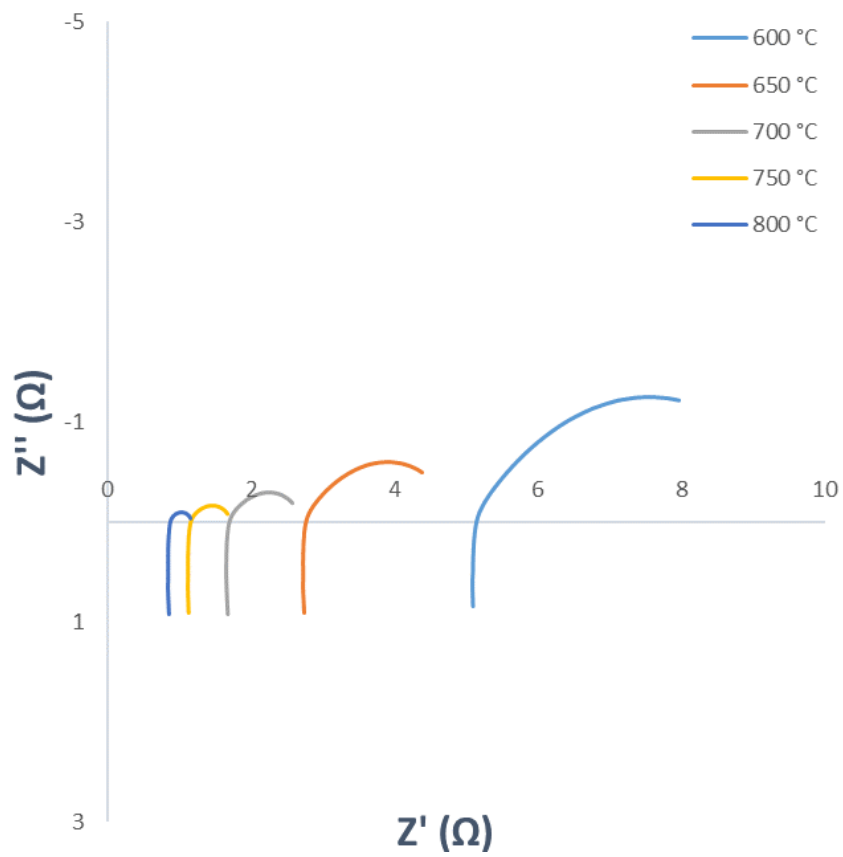


Figure 33 - EIS spectra, Ag-YSZ-Ag sample, 100% O₂

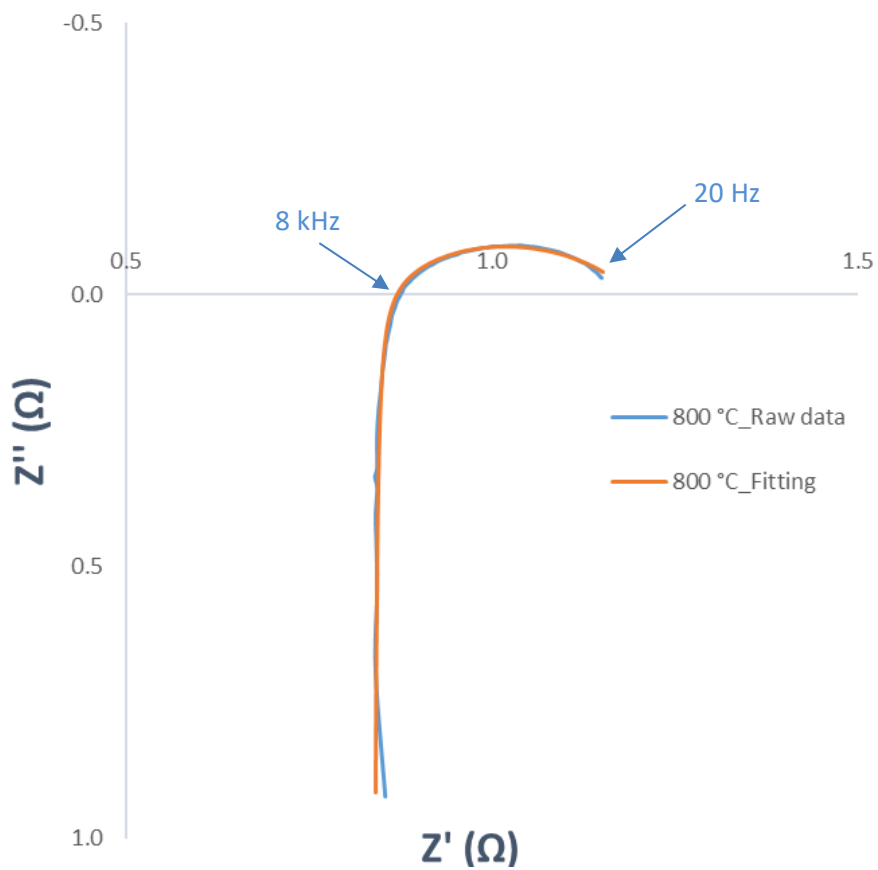


Figure 34 - EIS spectrum, Ag-YSZ-Ag sample, 800 °C and 100% O₂

The values of ohmic resistance and conductivity of the electrolyte for each temperature, obtained from the impedance data elaboration, are reported in Table 9.

Temperature [°C]	Ohmic resistance [Ω]	Conductivity [S/m]
600	5.06	0.651
650	2.72	1.21
700	1.64	2.00
750	1.12	2.94
800	0.837	3.93

Table 9 - Ohmic resistance and conductivity of the electrolyte, Ag-YSZ-Ag sample, 100% O₂

The results were collected to produce the Arrhenius plot (Figure 35). What can be observed is analogous to what observed with the 100% N₂ atmosphere: the conductivity increases with the temperature and follows the Arrhenius trend. The area affected by the wires in the Arrhenius plot can appear larger, but this is due to the fewer temperature levels that have been investigated.

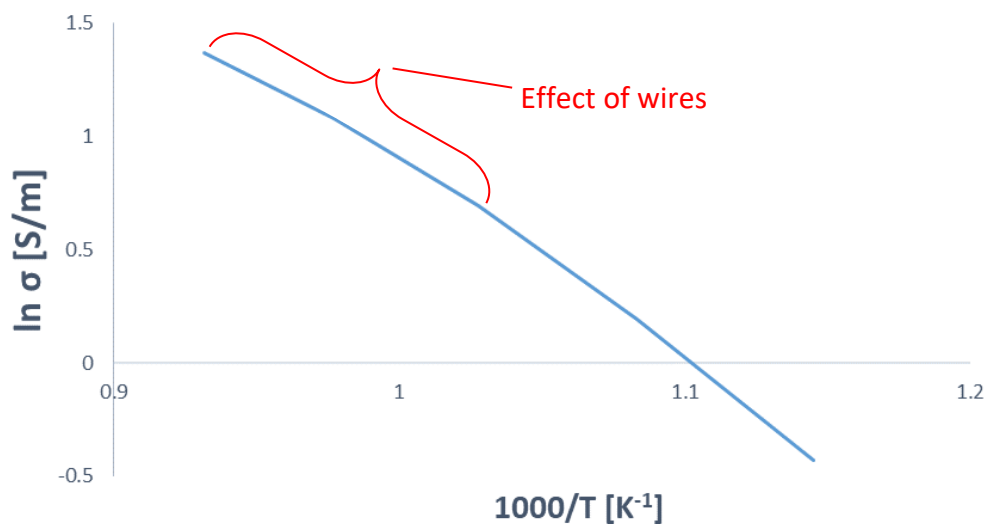


Figure 35 - Arrhenius plot, Ag-YSZ-Ag sample and 100 % O₂

5.1.1.2. LSM|YSZ|LSM sample

For the LSM|YSZ|LSM sample the electrolyte resulted 0.973 mm thick and the electrode area of 2.01 cm².

- 100% N₂ atmosphere

The EIS spectra for the N₂ atmosphere are shown in Figure 36. It can be immediately noticed that with increasing temperature the total impedance response decreases. Moreover, after a certain threshold, around 550 °C, the reduced impedance is more evident. For this reason, the spectra at higher temperatures are not well distinguishable from the chart, and this is why an enlargement of the 800 °C impedance curve is represented in Figure 37, taken as representative of that region. Once again, the disordered behavior of the data occurs at the lower temperatures.

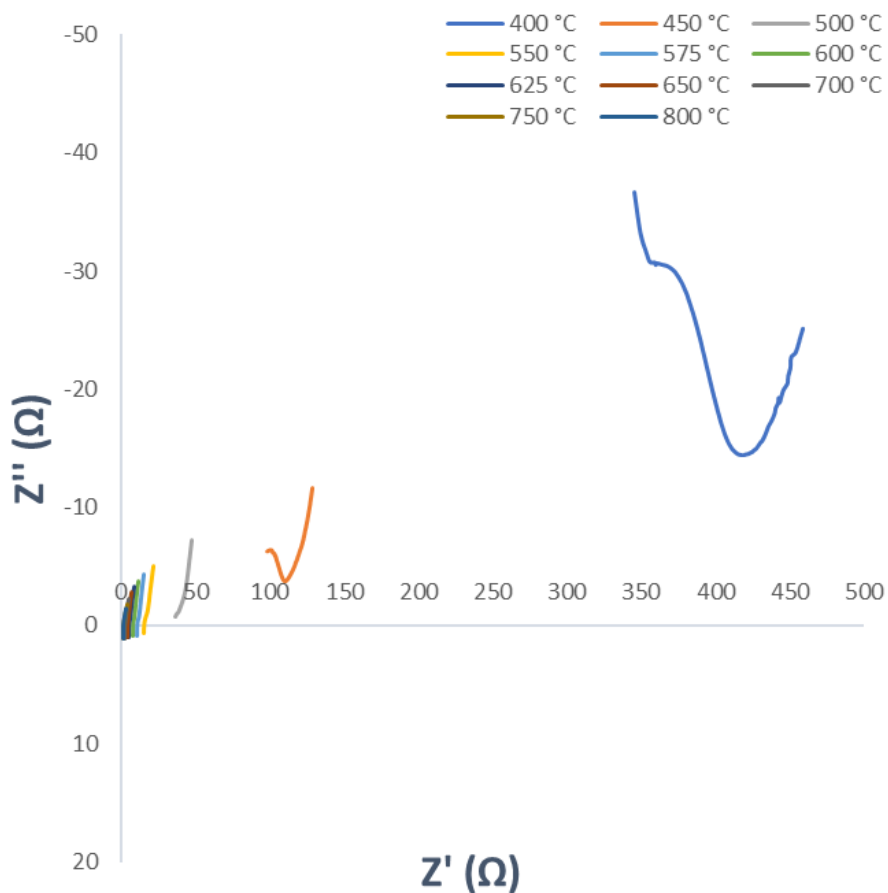


Figure 36 - EIS spectra, LSM-YSZ-LSM sample, 100% N₂

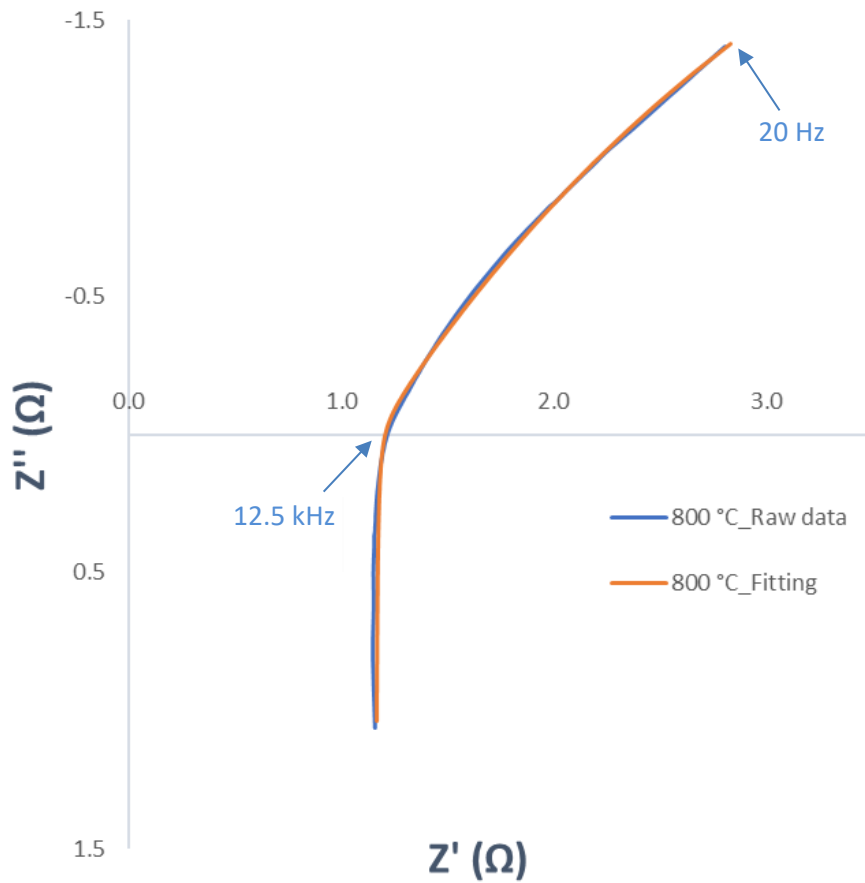


Figure 37 - EIS spectrum, LSM-YSZ-LSM sample, 800 °C and 100% N_2

The values of ohmic resistance and conductivity of the electrolyte for each temperature, obtained from the impedance data elaboration, are reported in Table 10.

Temperature [°C]	Ohmic resistance [Ω]	Conductivity [S/m]
400	388	0.0125
450	110	0.0440
500	32.4	0.149
550	14.5	0.334
575	10.0	0.482
600	7.15	0.677
625	5.21	0.929
650	3.87	1.25
700	2.35	2.06
750	1.59	3.05
800	1.16	4.18

Table 10 - Ohmic resistance and conductivity of the electrolyte, LSM-YSZ-LSM sample, 100% N₂

This concludes the analysis at 100% N₂ atmosphere for this sample, the Arrhenius plot could be plotted in Figure 38. As expected, the conductivity decreases with decreasing temperature and follows the Arrhenius trend. Besides the part at very high temperature that is affected by the wires, there is another point of slope change at intermediate temperature. This is the impact of modified conductivity mechanism of LSM electrode. However, further dissemination of such phenomenon is beyond the scope of this thesis. Additional information can be found in [50].

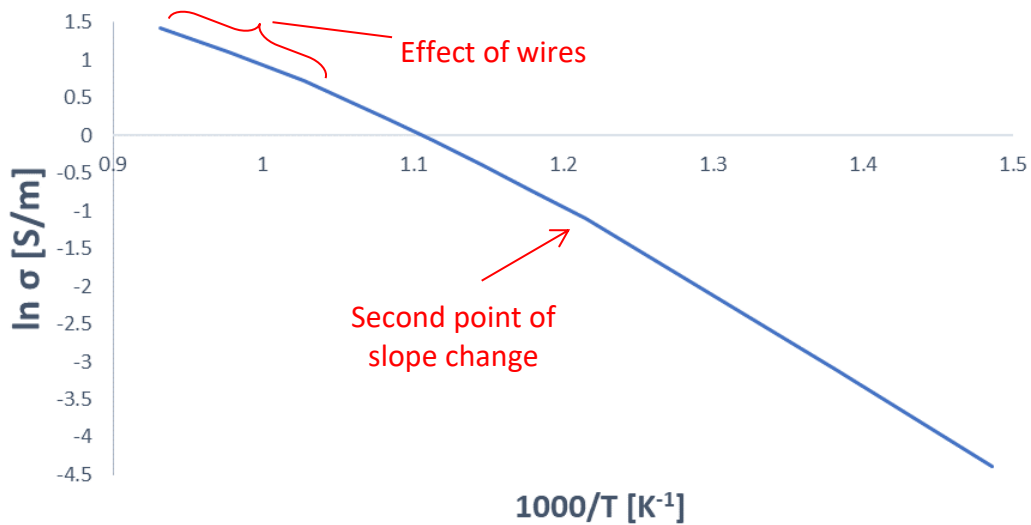


Figure 38 - Arrhenius plot, LSM-YSZ-LSM sample and 100 % N₂

- 100% O₂ atmosphere

The EIS spectra for the O₂ atmosphere are shown in Figure 39. Analogously to the N₂ atmosphere, higher temperature leads to a lower total impedance response, with such a behavior more evident after a certain threshold, around 550 °C. For this reason, the spectra at higher temperatures are not well distinguishable from the chart, and this is why an enlargement of the 800 °C impedance curve is represented in Figure 40, taken as representative of that region. Once again, the disordered behavior of the data occurs at the lower temperatures.

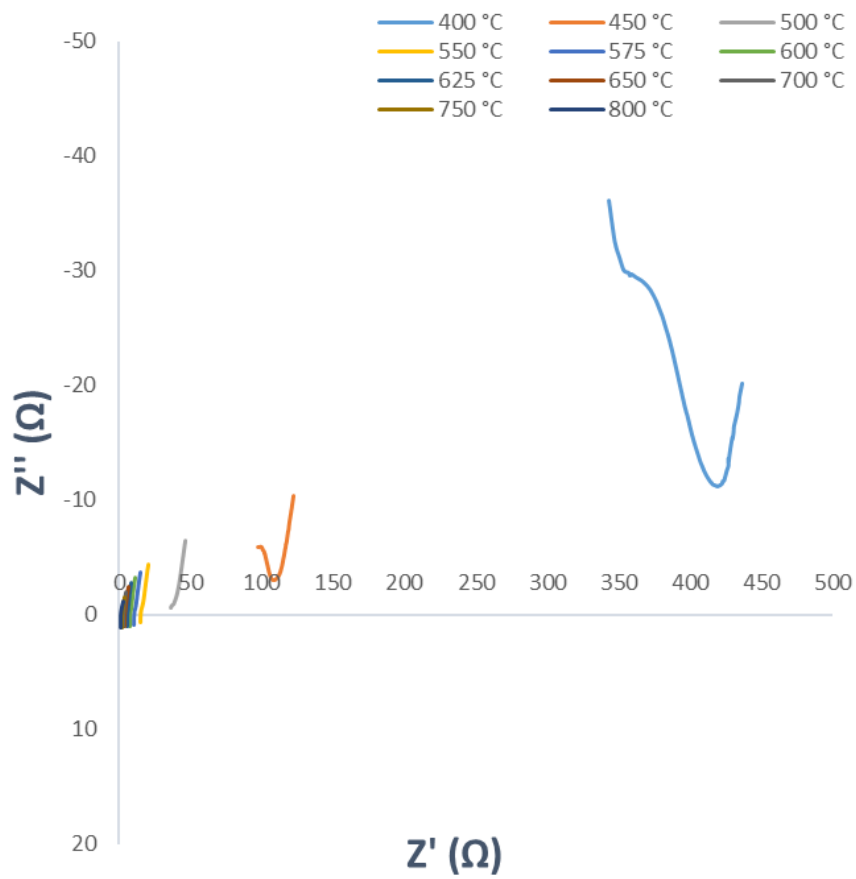


Figure 39 - EIS spectra, LSM-YSZ-LSM sample, 100% O₂

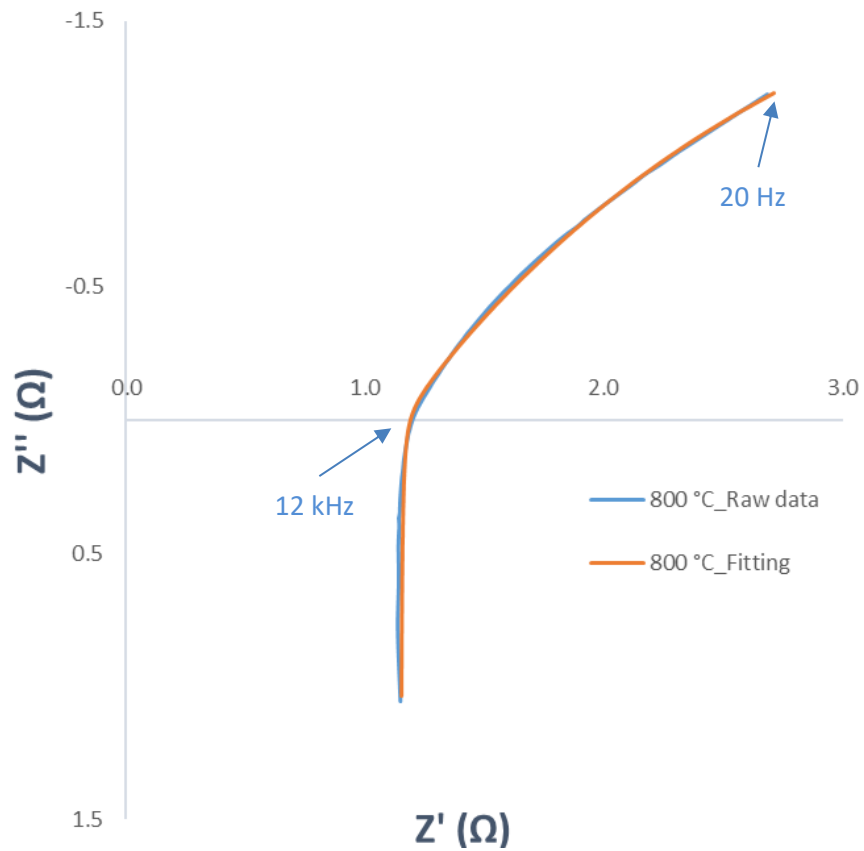


Figure 40 - EIS spectrum, LSM-YSZ-LSM sample, 800 °C and 100% O₂

The values of ohmic resistance and conductivity of the electrolyte for each temperature, obtained from the impedance data elaboration, are reported in Table 11.

Temperature [°C]	Ohmic resistance [Ω]	Conductivity [S/m]
400	404	0.0120
450	109	0.0443
500	33.9	0.143
550	14.5	0.333
575	10.0	0.483
600	7.07	0.685
625	5.22	0.928
650	3.89	1.25
700	2.38	2.03
750	1.57	3.08
800	1.14	4.23

Table 11 - Ohmic resistance and conductivity of the electrolyte, LSM-YSZ-LSM sample, 100% O₂

This was the last experiment regarding the measurement of conductivity for the compressed powder-based electrolyte. The Arrhenius plot for the 100% O₂ atmosphere of the LSM|YSZ|LSM sample is presented in . As expected, the conductivity decreases with decreasing temperature and follows the Arrhenius trend, apart from the region affected by the wires and some minor errors due to the data evaluation, inner conductivity mechanism of LSM or experimental error.

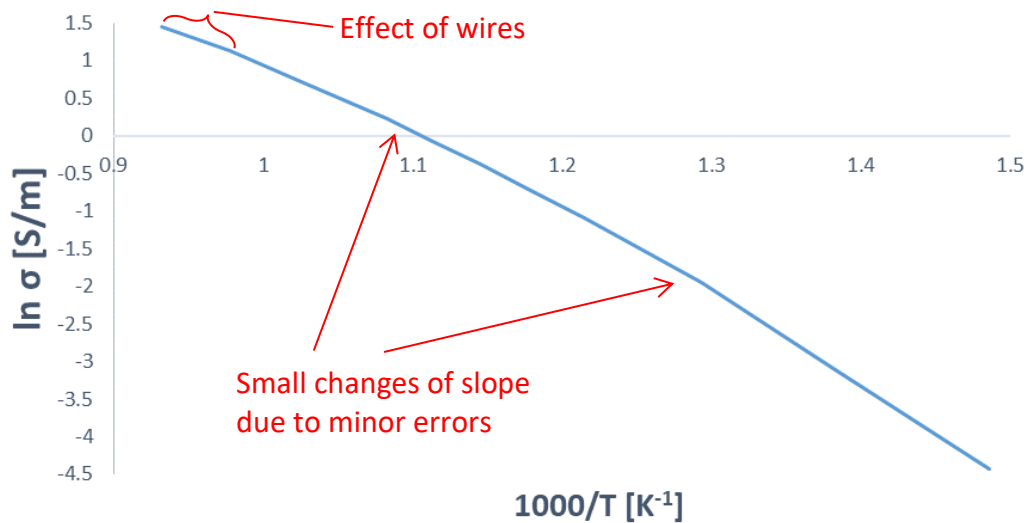


Figure 41 – Arrhenius plot, LSM-YSZ-LSM sample and 100 % O₂

- Comparison of the compressed powder-based electrolytes

Completed all the conductivity experiments on the compressed powder-based electrolyte in the various conditions, it was possible to compare the results and indagate the effect of the different types of electrodes and gas composition on the electrolyte's conductivity. To do so, the four Arrhenius plots previously produced were plotted on the same chart. It is represented in Figure 42. What emerges is that the conductivity of the electrolyte does not depend on the type of electrodes deposited on it, as well as it does not depend on the gas compositions it is subjected to. This confirmed our initial expectations because such changes should not impact the conductivity if each used material is stable at the applied experimental conditions.

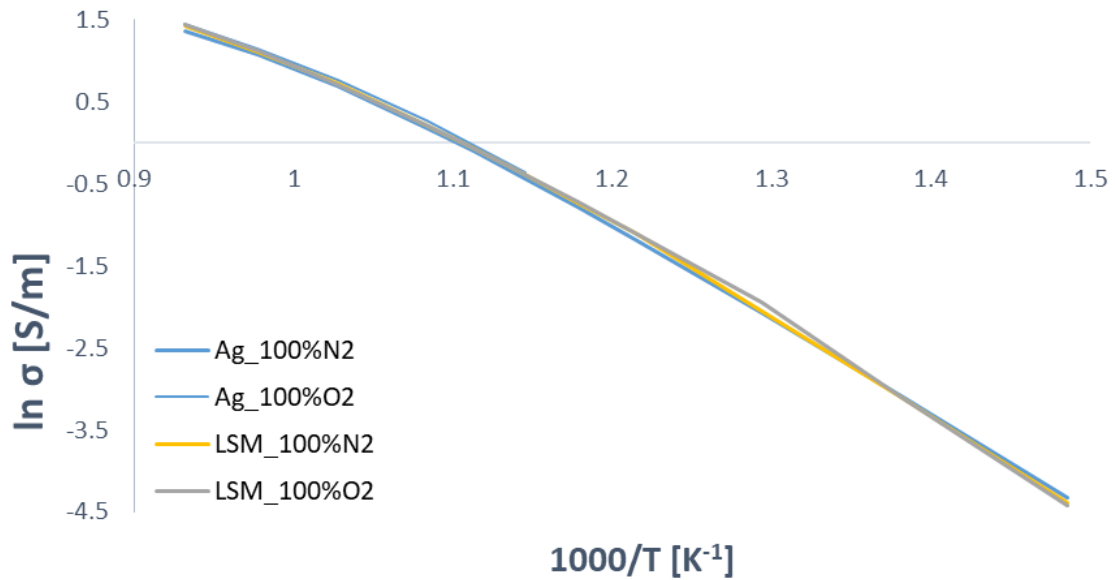


Figure 42 - Comparison of the Arrhenius plots of the compressed powder-based electrolyte cells tested in different conditions

5.1.2. Electrochemical characterization

Although the main focus of this thesis is the YSZ electrolyte, an experiment about the behavior of a complete cell was carried out, focused on a symmetrical LSM|YSZ|LSM three-electrode assembly. From the experimental results, the specific current was calculated simply by dividing by the electrode area, while the overpotential was calculated through Eq. 8. The electrode area resulted to be 2.01 cm² wide.

At this point, the j - V curve and the j - η curve were produced for the different temperature levels. The curves related to the two different gas compositions considered were plotted on the same chart to make their comparison easier. The charts will be shown in the next lines. If needed, the numerical results are available in the appendix.

- 800 °C

The j - V and the j - η curve are shown in Figure 43 and Figure 44, respectively.

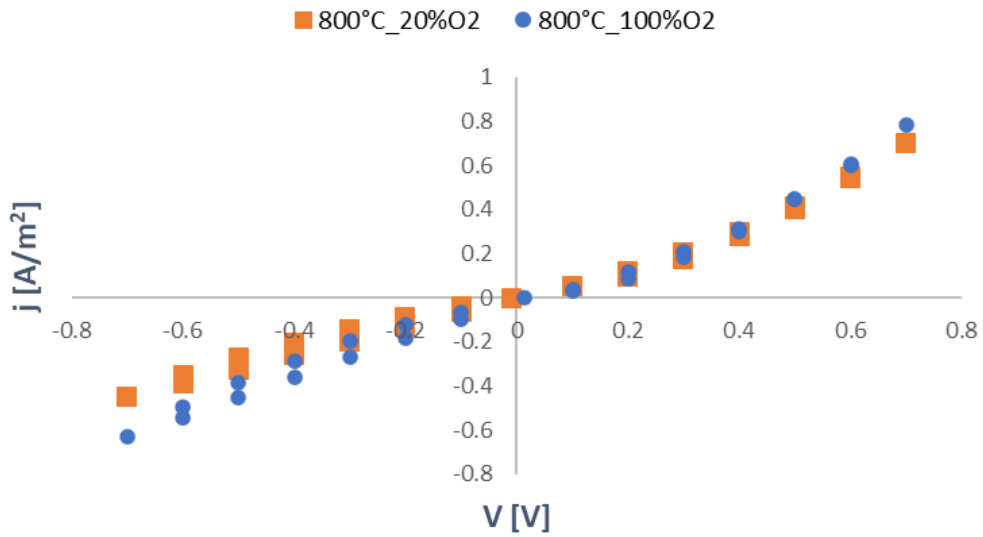


Figure 43 - j - V curve, 3-electrode assembly cell, 800 °C, 100% O₂ and 20% O₂

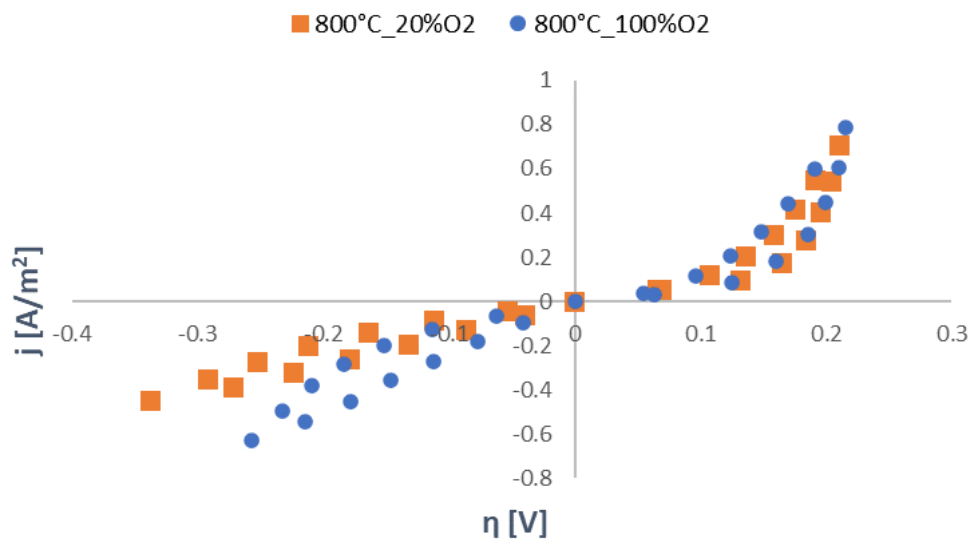


Figure 44 - j - η curve, 3-electrode assembly cell, 800 °C, 100% O₂ and 20% O₂

- 700 °C

The j - V and the j - η curve are shown in Figure 45 and Figure 46, respectively.

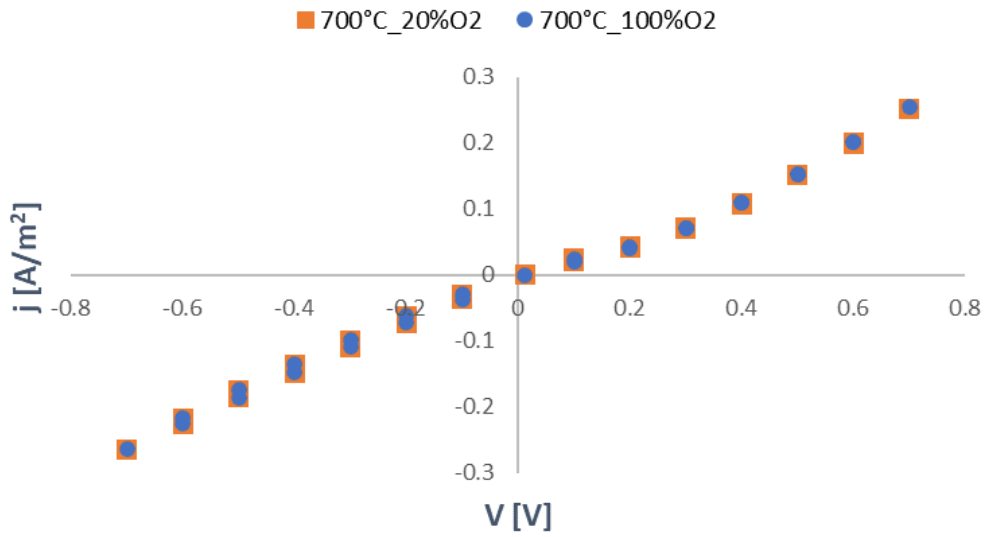


Figure 45 - j - V curve, 3-electrode assembly cell, 700 °C, 100% O₂ and 20% O₂

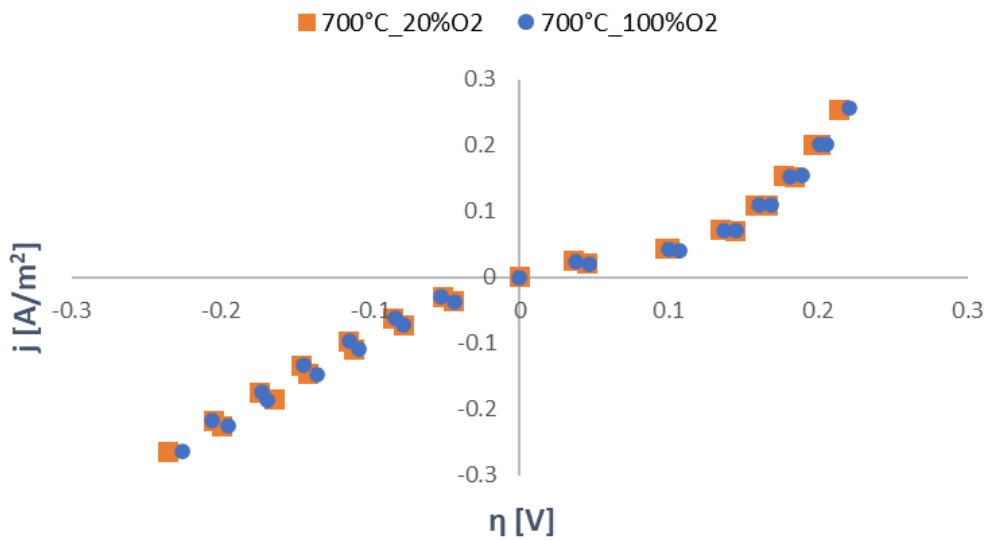


Figure 46 - j - η curve, 3-electrode assembly cell, 700 °C, 100% O₂ and 20% O₂

- 600 °C

The j - V and the j - η curve are shown in Figure 47 and Figure 48, respectively.

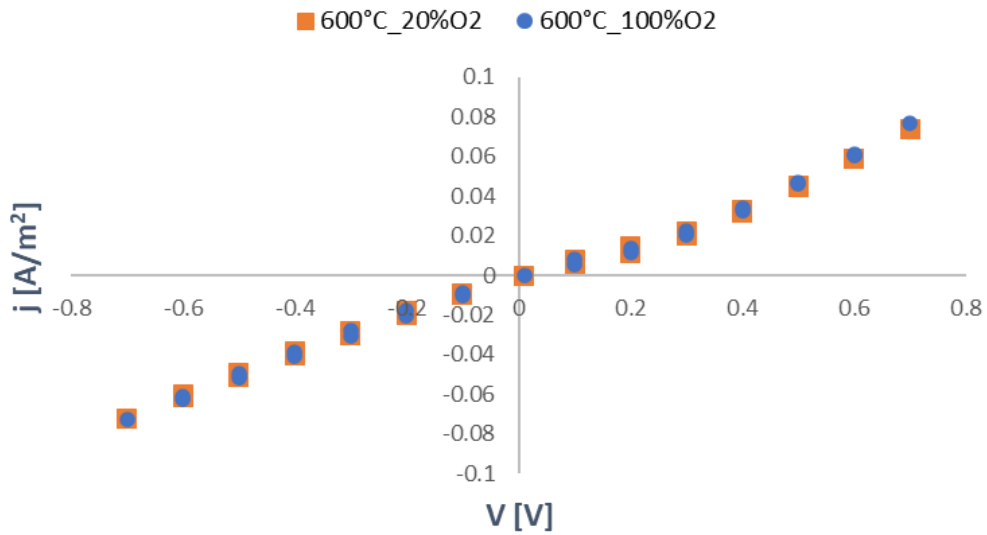


Figure 47 - j - V curve, 3-electrode assembly cell, 600 °C, 100% O₂ and 20% O₂

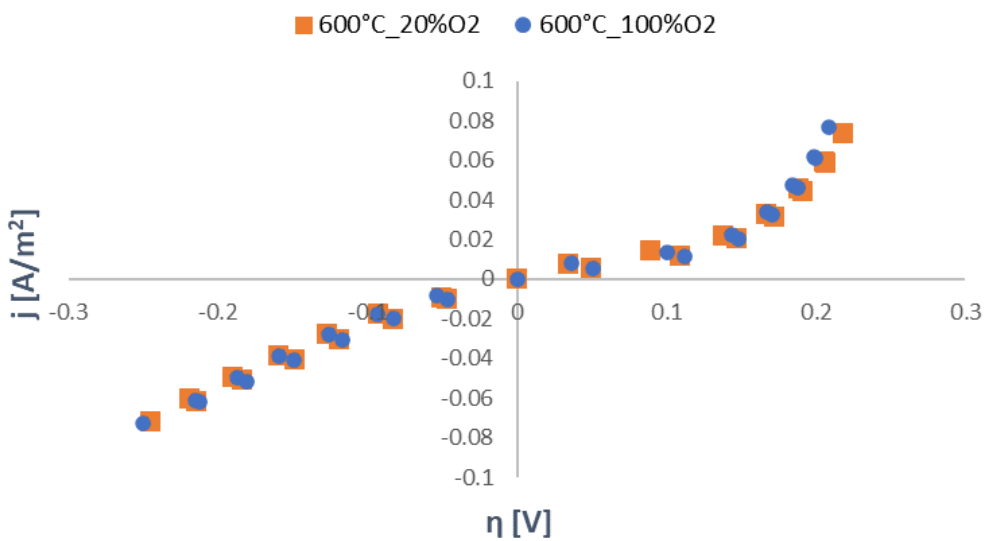


Figure 48 - j - η curve, 3-electrode assembly cell, 600 °C, 100% O₂ and 20% O₂

From the curves can be noticed as the performances of the cell worsen decreasing the operational temperature. Moreover, at 800 °C, the oxygen reduction reaction rate is faster at O₂ rich atmosphere, while this does not happen

for the other temperatures. The oxygen evolution reaction rate results not dependable on the gas atmosphere for all the three temperature levels.

5.2. Slurry casted electrolyte

Since the slurry casting procedure had not been optimized yet, several attempts were made to fabricate the electrolyte of desired properties. The most important properties that the electrolyte should feature are high ionic conductivity, poor electrical conductivity, gas tightness, thermal and mechanical stability and durability.

The first sample produced, also taken as reference for the optimization, was characterized by the base case slurry composition, 500 μm slit height and 1360 $^{\circ}\text{C}/6\text{h}$ sintering. It was 0.55 mm thick, white and very fragile. The XRD analysis resulted in a pure YSZ cubic phase. From the photomicrographs in Figure 49, a residual high porosity can be noticed, characterized by the presence of significant void space. This evidence put the focus of the optimization process on the reduction of such porosity. Apart from this, the electrolyte seemed promising, presenting fair connections among the sintered particles.

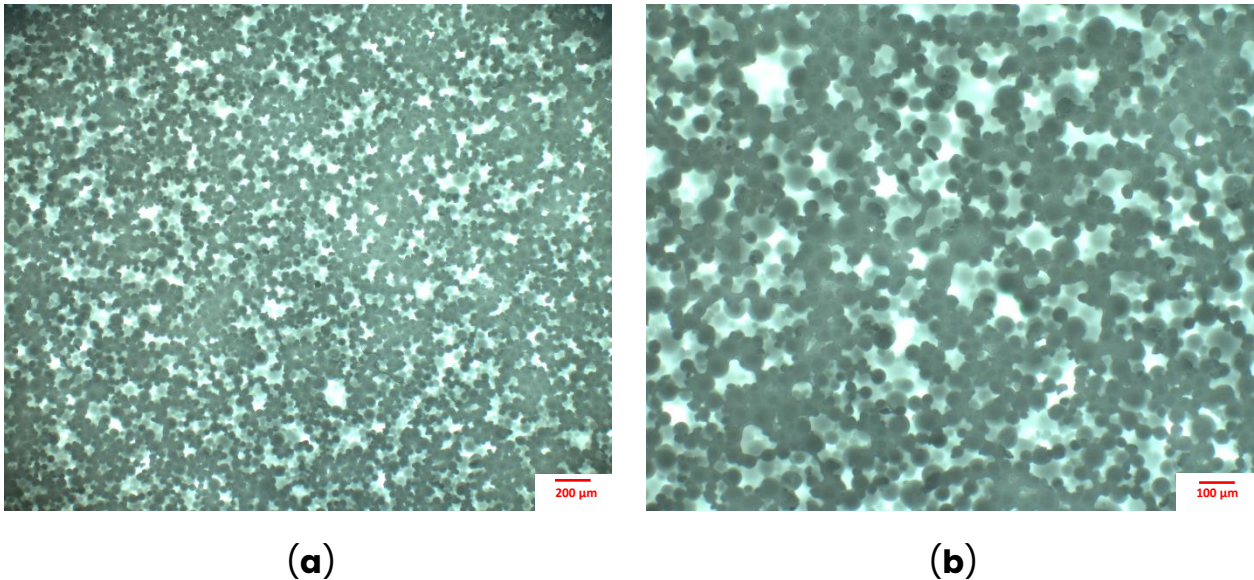


Figure 49 - Photomicrographs of the reference slurry casted electrolyte at different magnifications, after the sintering: (a) 10x; (b) 20x

The modifications that were applied on the reference electrolyte interested the slurry composition, the sintering settings and the slit height. All of them principally aimed at the reduction of the porosity and bolstering the mechanical integrity. Such modifications are listed below:

- Slurry composition
 - +25%, +35%, +50% YSZ powder
 - -25%, -35%, -50% PVB binder
- Sintering temperature and time
 - 1360 °C/6 h (sintering protocol 1 of Appendix table I)
 - 1550 °C/24 h (sintering protocol 2 of Appendix table I)
- Slit height
 - 250 μm
 - 500 μm
 - 750 μm
 - 1000 μm

Some of the modifications were also applied at the same time to utilize their synergistic effect. The effects on the final product were detected with different approaches: while in some cases the SEM or the optical microscopy were employed, in most cases the simple visual analysis was sufficient to understand what was going on. Of course, deeper and more precise analysis would be preferable but, given the huge number and apparent results of samples produced, it was not feasible to follow this direction for all of them.

The first change to the procedure was done on the slit height: 250, 750 and 1000 μm height were also applied, besides the previously used 500 μm , keeping the slurry composition and the settings of the sintering unchanged. The photomicrographs of the fabricated electrolytes are shown in Figure 50. The main result was that the 250 μm slit height produces too thin and fragile electrolytes, while the remaining samples were still promising. Therefore, now on, the 250 μm slit height was not considered anymore, while the other ones were employed in combination with different modifications.

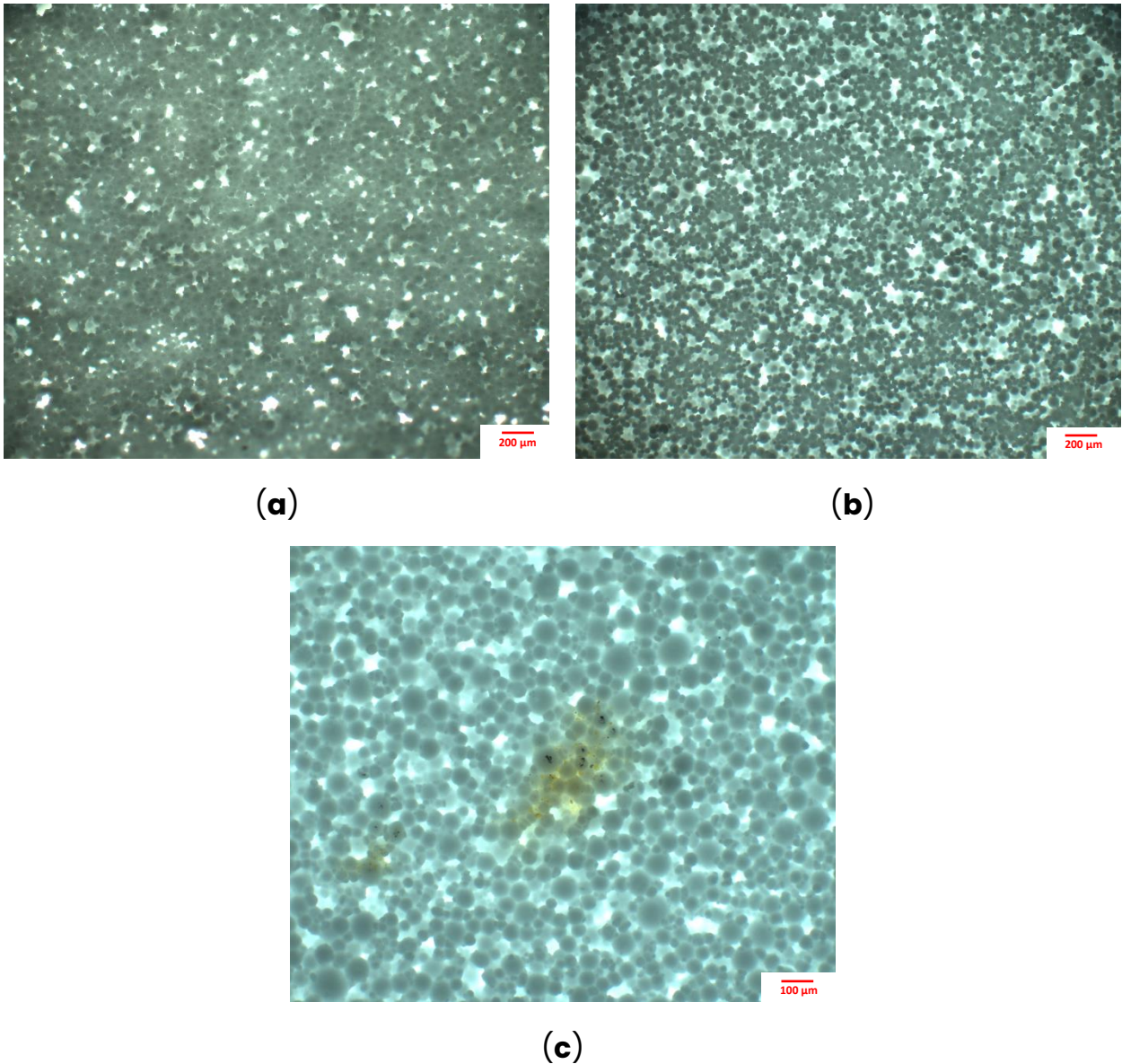


Figure 50 - Photomicrographs of electrolytes produced with different slit height: (a) 250 μm; (b) 750 μm; (c) 1000 μm

At this point, the effect of a higher temperature and a longer time sintering was tested: 1550 °C/24 h instead of 1360 °C/6h. These new settings in the sintering were combined with 500, 750 and 1000 μm slit height and reference slurry composition. The photomicrographs, that were produced only for the 500 and 1000 μm slit heights, are shown in Figure 51. Comparing with the sintering at lower temperature, the electrolytes seemed sintered better and, consequently, less porous. Nevertheless, both the sintering settings were kept in the following

experiments, to verify their effect in combination with other modifications of the fabrication procedure.

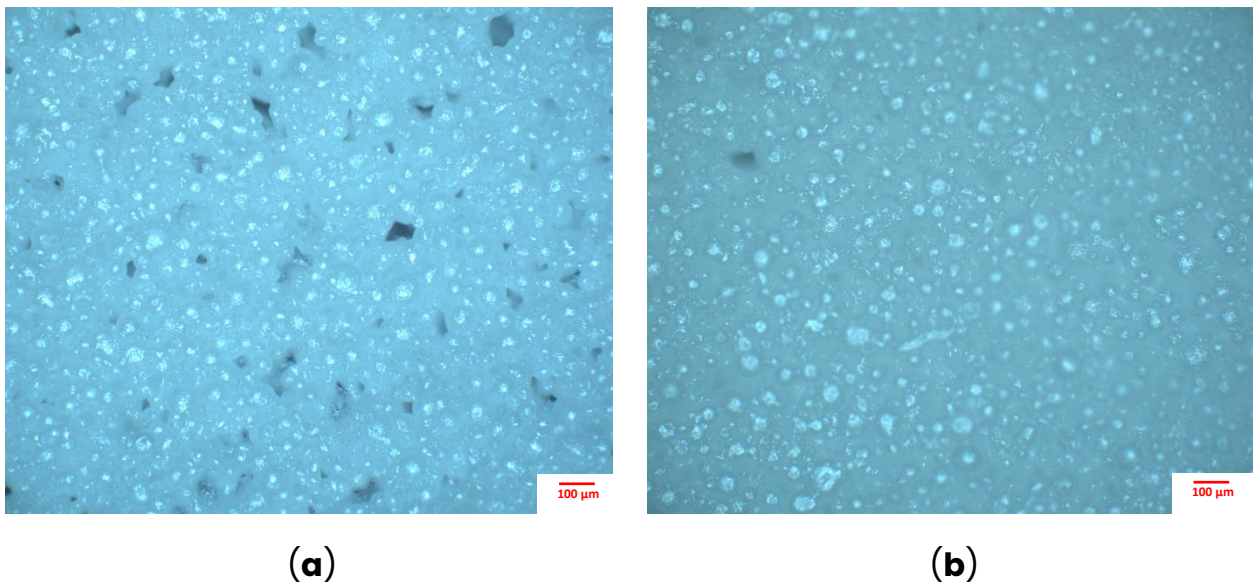


Figure 51 - Photomicrographs of electrolytes produced with 1550 °C/24h sintering and different slit height: (a) 500 μm; (b) 1000 μm

After these first manufacturing alterations the attention was moved on the composition of the slurry. For easier comprehension, the characteristics of each slurry composition produced are summarized in Table 12. Firstly, one batch with 25% more YSZ powder (batch 1) and one with 50% more YSZ powder (batch 2), with respect to the reference, were produced. 500, 750 and 1000 μm slit heights were employed. The slurry with 50% more powder presented a lot of clumps and a very viscous consistency. For this reason, was not possible to produce a proper tape with the 1000 μm slit height of the doctor blade (see Figure 52). For the rest, the tapes were correctly casted and two stripes were obtained from each of them, sintering one at 1360 °C/6h and one at 1550 °C/24h. The final products seemed good and, by visual inspection, the ones sintered at higher temperatures looked less porous. Therefore, for further analysis, the samples sintered at higher temperature were investigated by scanning electron microscopy. The SEM

images are shown in Figure 53 for the slurry with 25% more YSZ powder and in Figure 54 for the slurry with 50% more powder.

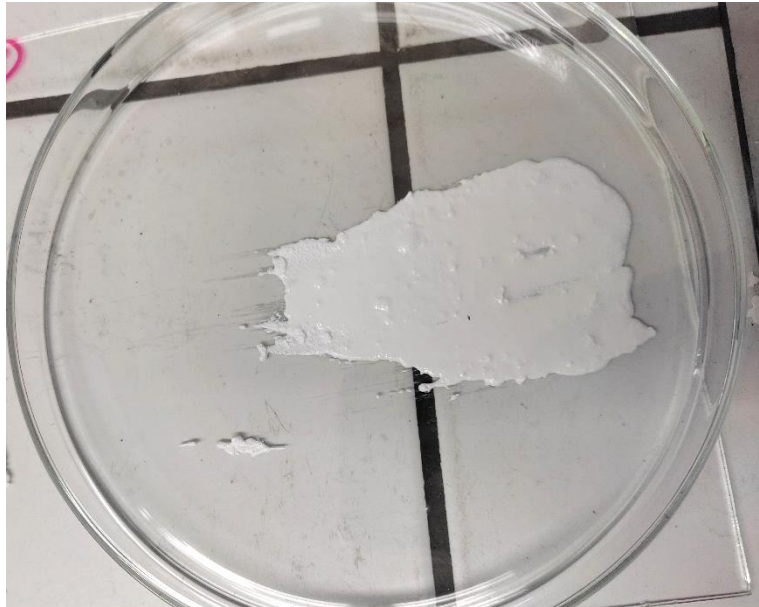
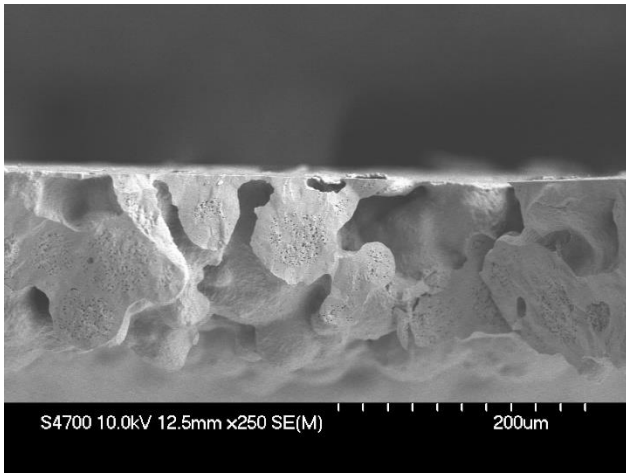
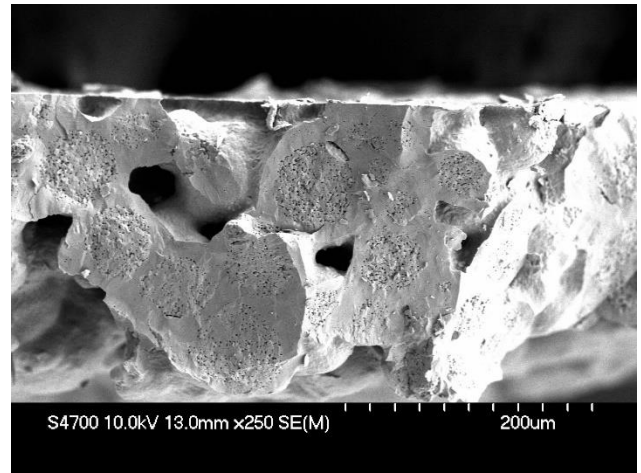


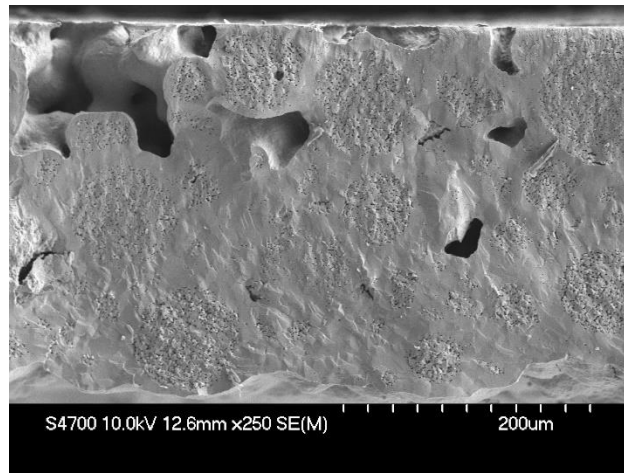
Figure 52 - Casted tape from slurry with +50% YSZ powder, 1000 μm slit height



(a)



(b)



(c)

Figure 53 - SEM images of electrolytes produced with 1550 °C/24h sintering, +25% YSZ powder and different slit height: (a) 500 μm ; (b) 750 μm ; (c) 1000 μm

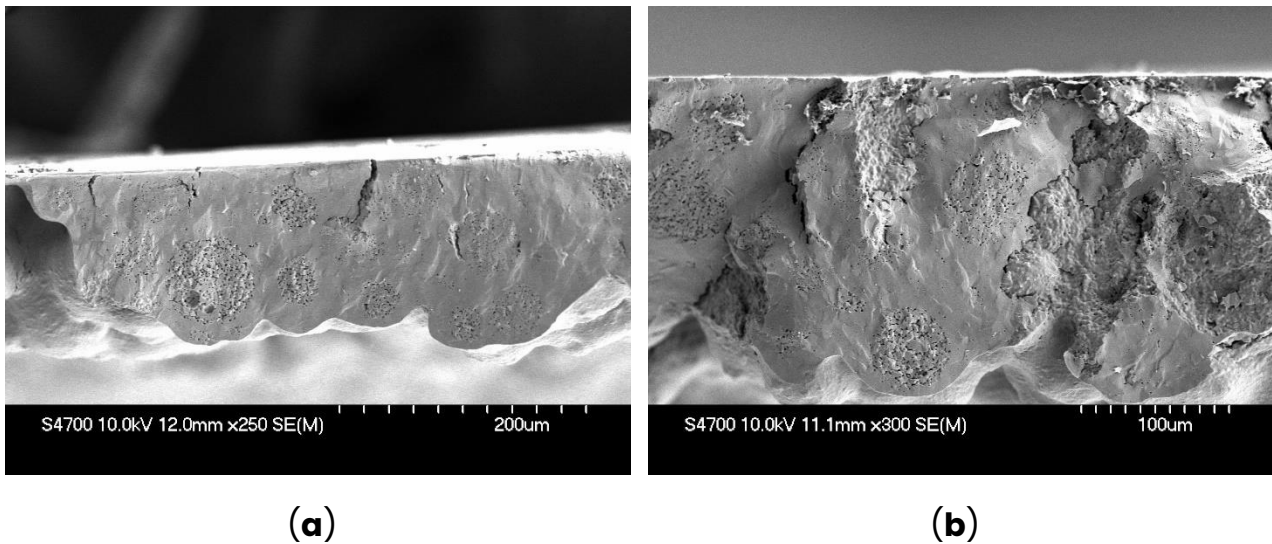


Figure 54 - SEM images of electrolytes produced with 1550 °C/24h sintering, +50% YSZ powder and different slit height: **(a)** 500 μm; **(b)** 750 μm

The SEM images put in evidence how the porosity was still present and the necessity to keep trying alternative procedures. Anyway, they also suggested that a higher slit height could be more beneficial than a lower one, as can be found in Figure 53 - c, that results to be, so far, the closest to the target.

On the lines of the latest attempt, other slurry compositions were produced. One batch featured a 25% reduction of the content of the PVB binder (batch 3), another one a 50% reduction of PVB binder (batch 4), a third one a combination of 25% more YSZ powder and 25% less PVB binder (batch 5) and a fourth one a combination of 35% more YSZ powder and 35% less PVB binder (batch 6).

Batch 3 was casted at 500, 750 and 1000 μm slit height. Due to the less amount of binder in it, the slurry was more liquid and was easier to cast it. Batch 4 was even more liquid, as could be expected, making difficult to cast at 500 and 750 μm slit heights and impossible to cast at 1000 μm. Batch 5 and batch 6 were casted at 750 and 1000 μm.

Two stripes were produced from each tape: one for sintering at 1360 °C/6h and one for sintering at 1550 °C/24h. At the end of the sintering process, the stripes

from batch 4, 750 μm slit height and 1550 $^{\circ}\text{C}$ sintering resulted cracked and were therefore discarded. The remaining stripes produced from batch 3 and 4 which were sintered at 1550 $^{\circ}\text{C}$ were analyzed by SEM (Figure 55). The sintered stripes produced from batch 5 and 6 were analyzed just by eye and did not suggest any significant improvement but, on the contrary, the stripes from batch 6 were plenty of clumps, probably due to the higher amount of YSZ powder.

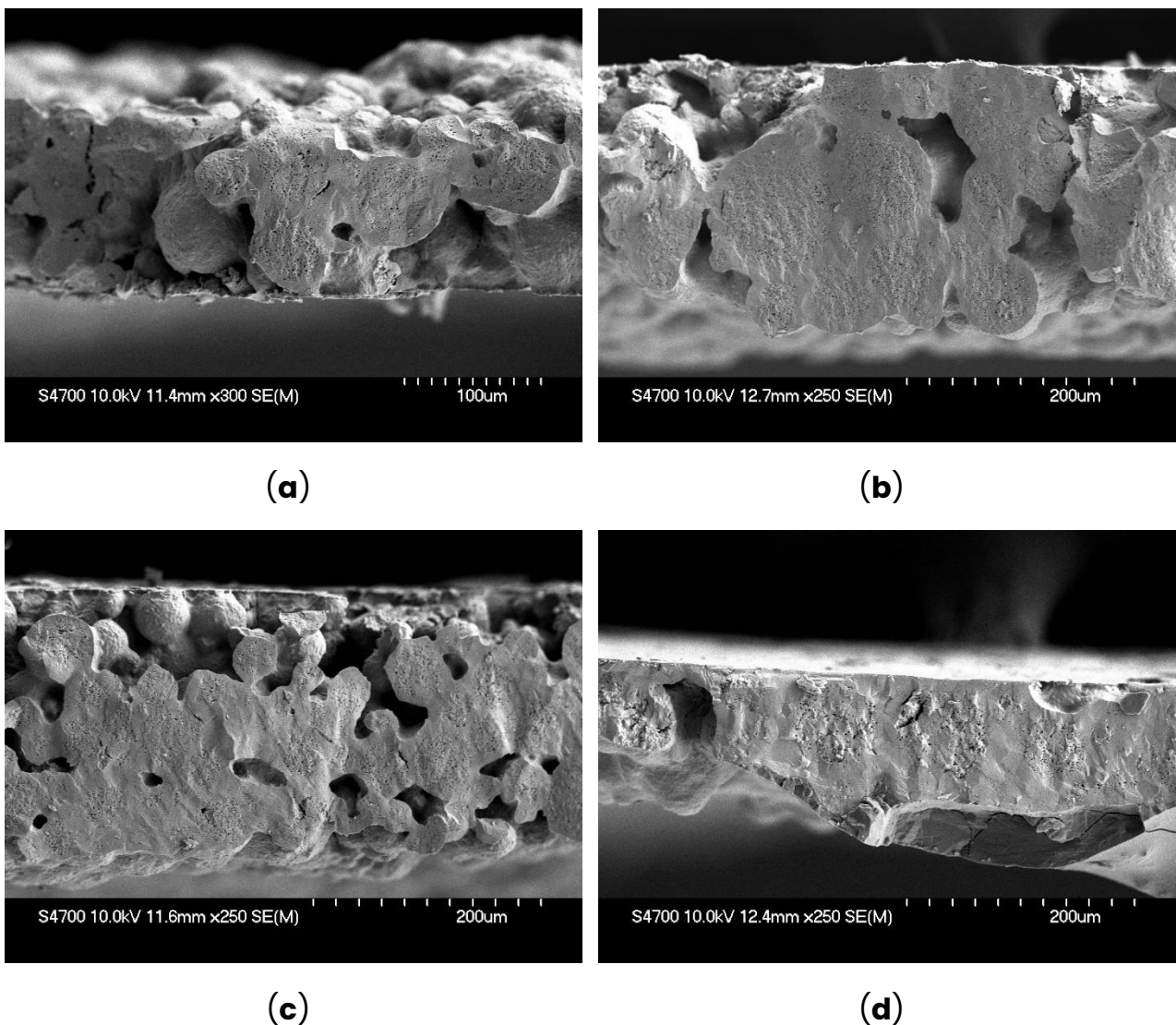


Figure 55 - SEM images of electrolytes produced with 1550 $^{\circ}\text{C}/24\text{h}$ sintering, different slurry composition and different slit height: (a) Batch 3, 500 μm ; (b) Batch 3, 750 μm ; (c) Batch 3, 1000 μm ; (d) Batch 4, 500 μm

Batch	Characteristics compared to reference sample
1	+25% YSZ powder
2	+50% YSZ powder
3	-25% PVB binder
4	-50% PVB binder
5	+25% YSZ powder and -25% PVB binder
6	+50% YSZ powder and -50% PVB binder

Table 12 - Characteristics of the produced slurries with respect to the reference one

To sum up what was obtained so far, it was seen how higher slit height, higher sintering temperature and time and higher amount of YSZ powder in the slurry may be beneficial for the improvement of the electrolyte's characteristics. Nonetheless, the modification applied so far were not able to completely overcome the problem regarding the porosity. For this reason, a new approach was explored: to try to fill the pores by applying a layer of a chemical solution containing YSZ powder on the already tape casted samples. Three different solutions were prepared, composed by the following elements:

- Solution A: 2 g of YSZ powder and 2 ml of Terpeneol
- Solution B: 2 g of YSZ powder and 1.4 ml of Ethylene glycol
- Solution C: 2 g of YSZ powder and 1.5 ml of Glycerol

Each solution underwent 30 minutes of ultrasound bath before their application. The solutions were deposited individually, by means of a brush. They were applied to three different samples: a not sintered stripe produced with the reference procedure, a not sintered stripe produced with 25% less content of PVB binder and

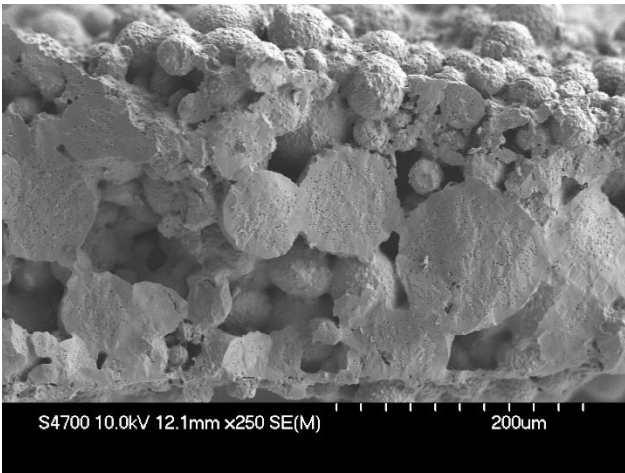
on a sintered stripe produced with 25% less content of PVB binder. The slit height was 750 μm for all the samples. To enhance the absorption of the solution the stripes were put to rest for 10 minutes in a vacuum drier (shown in Figure 56) at 50 kPa. The solutions were deposited on one side of a stripe, then the stripe was dried at 100 $^{\circ}\text{C}$ for 5 minutes in an infrared IC heater, and the procedure was repeated for the other side.

Another attempt was done putting the 25% less PVB binder slurry at rest for 10 minutes in the 50 kPa vacuum drier before casting a tape, using a 750 μm slit height. This last alternative aimed at trying to remove eventual air bubbles trapped in the slurry that could be possibly responsible for the pores in the sintered electrolyte.

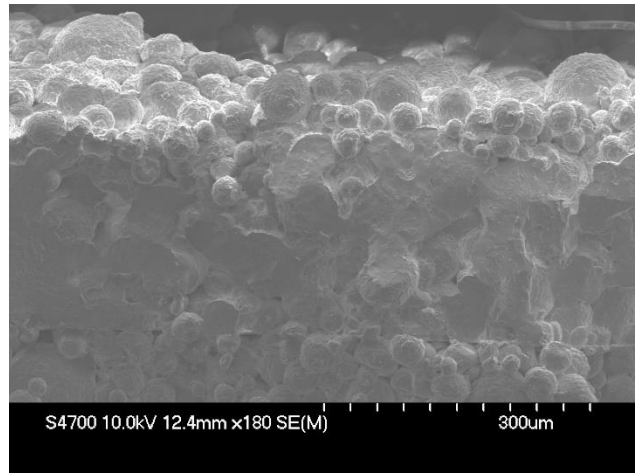
Solution A proved immediately to be not suitable because it dissolved the stripes once deposited. On the other hand, all the other samples were sintered at 1550 $^{\circ}\text{C}/24\text{h}$ and analyzed by means of SEM (Figure 57).



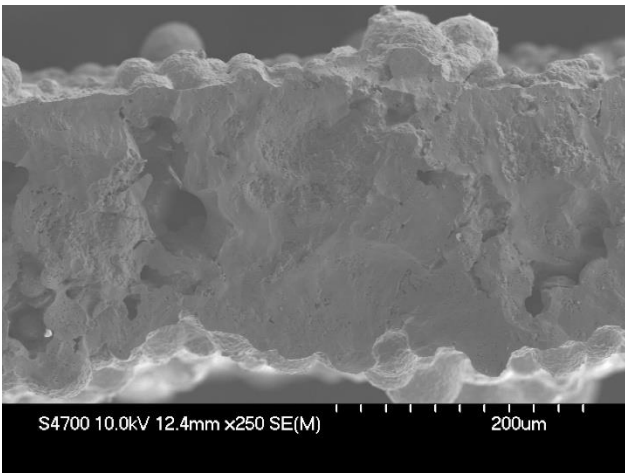
Figure 56 - Vacuum drier connected to a vacuum pump



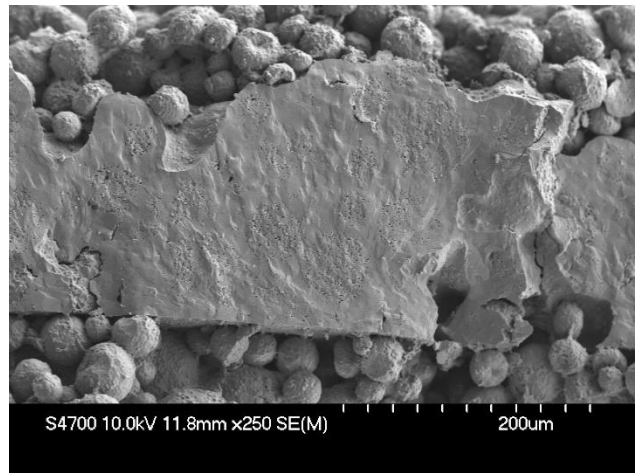
(a)



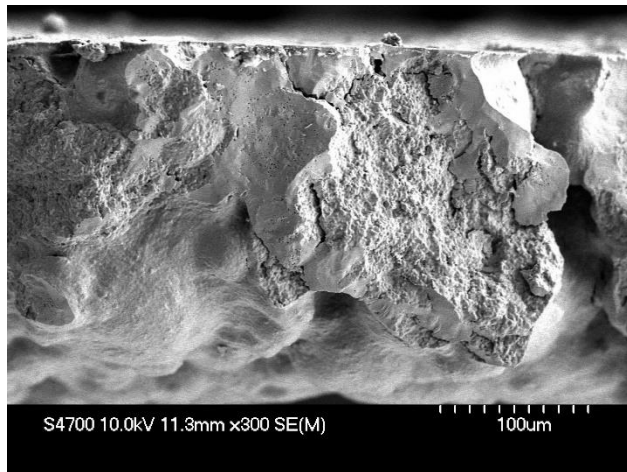
(b)



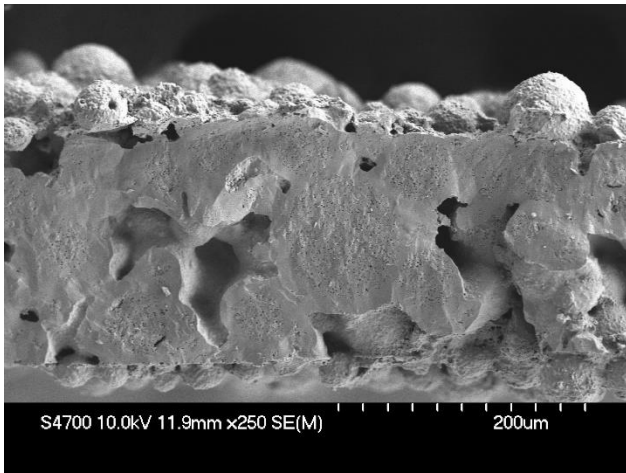
(c)



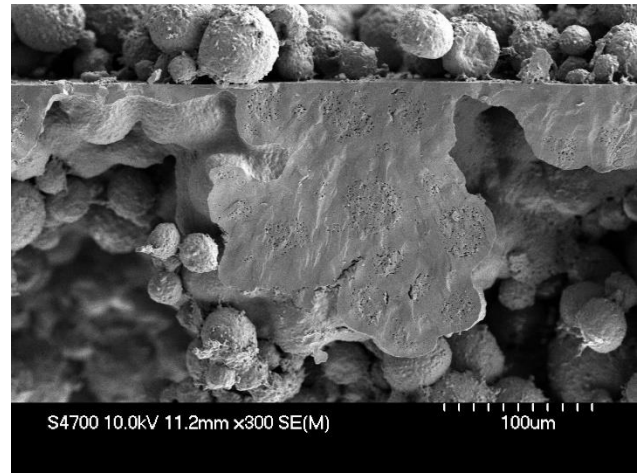
(d)



(e)



(f)



(g)

Figure 57 - SEM images: **(a)** solution B, reference procedure, not sintered sample; **(b)** solution C, reference procedure, not sintered sample; **(c)** solution B, -25% PVB, not sintered sample; **(d)** solution C, -25% PVB, not sintered sample; **(e)** -25% PVB sample, sintered vacuumed slurry; **(f)** solution B, -25% PVB, not sintered sample; **(g)** solution C, -25% PVB, sintered sample

As observed in Figure 57, these alternatives did not bring any major improvements but, on the contrary, particles agglomerates can be noticed on the surface of the stripes treated with the chemical solutions that were not able to reach the inner pores. One promising sample, if the particles agglomerate on its surface are excluded, seems to be the one in picture Figure 57-d. It could be eventually interested by further analysis in the future, however such experiments were beyond the scope of this thesis due to the time limitations.

At this point, to try the removal of particle agglomerates and enhance the sintering of the electrolyte, the TZ-8YS YSZ powder used so far was replaced with the YSZ8-TC grade powder (supplied by fuelcellmaterials.com), characterized by finer particles, as highlighted by the particle size distribution chart in Figure 58. Initially, this new powder just replaced the previous one, keeping all the procedure identical to the reference one. The result was not good, because all the casted tapes were plenty of clumps. For this reason, the powder was pre-treated with a mortar and a pestle, again without any improvements. Finally, the pre-treatment

with the mortar was replaced by a pre-treatment with ultrasound horn (Figure 59): a solution of YSZ powder and ethanol was irradiated by the ultrasound horn for 30 minutes. This solution was then mixed with the remaining additives (PVB binder, toluene, Tergitol and diethyl phthalate), the produced slurry underwent 30 minutes ultrasound bath and was finally casted. Unfortunately, once again, the tapes presented a lot of clumps (see Figure 60) and also this alternative was finally discarded. Further investigation would be useful to understand why this time the system did not behave as expected. This was the last attempt performed to optimize the slurry casting procedure.

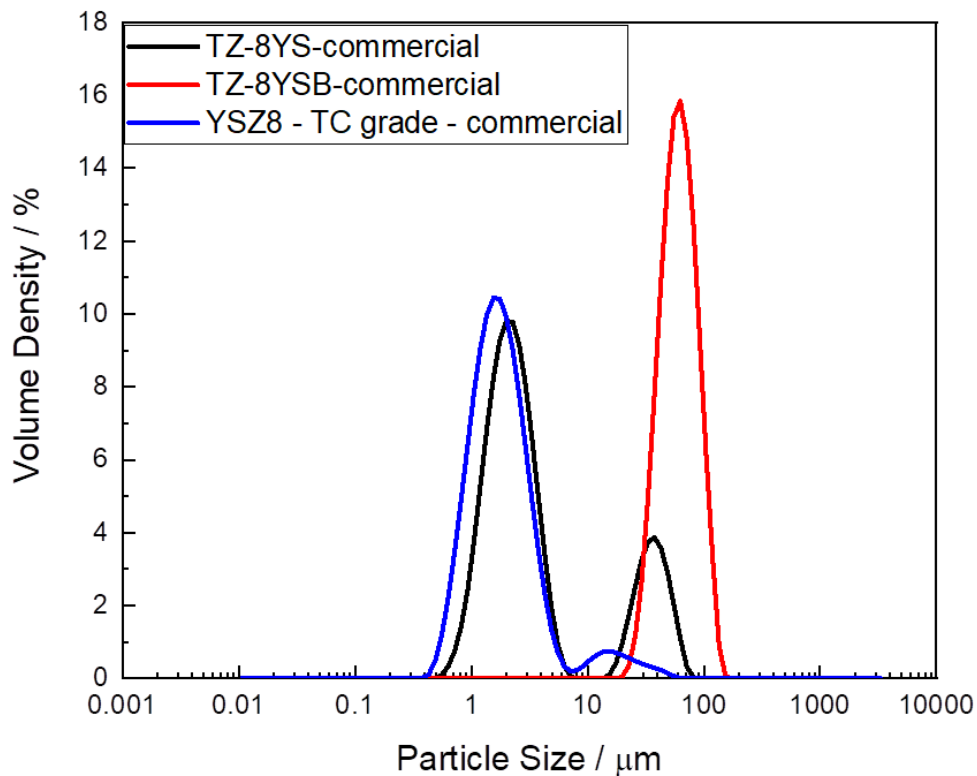


Figure 58 - Particle size distribution of different commercial YSZ powders



Figure 59 - Ultrasound horn pre-treatment



Figure 60 - Casted tapes plenty of clumps after ultrasound horn pre-treatment

To summarize, only minor improvements were obtained with respect to the reference procedure for the fabrication of the slurry casted electrolyte. The main defect, i.e. the porosity, is still present. Nevertheless, all the alternative routes undertaken have brought more knowledge and experience about the topic under research and some of them left space for further analysis and possible further

improvements in the future. Especially three routes seem the most promising: the one with incremented YSZ powder content, the one with combined increment of YSZ powder and decrement of PVB binder content and the one employing 8YSZ - TC grade powder. Moreover, it has also been verified that higher slit height and higher sintering temperature and time may be beneficial for the characteristics of the final product. An other possible improvement is represented by the automation of the casting process through the utilization of a tape caster. This machine, shown in Figure 61, allows to spread and cast the slurry on the glass in an automatic manner, programming the movement with the G-code. The tape caster, that offers a faster and more precise way to fabricate the electrolyte, was employed to produce just very few tapes that were not analyzed at all because it was available in the lab only in the very last period of the experimental work. To conclude, the slurry casted electrolyte was successfully fabricated but some work is still needed to make its characteristics more suitable for the function it has to cover in a solid oxide cell.

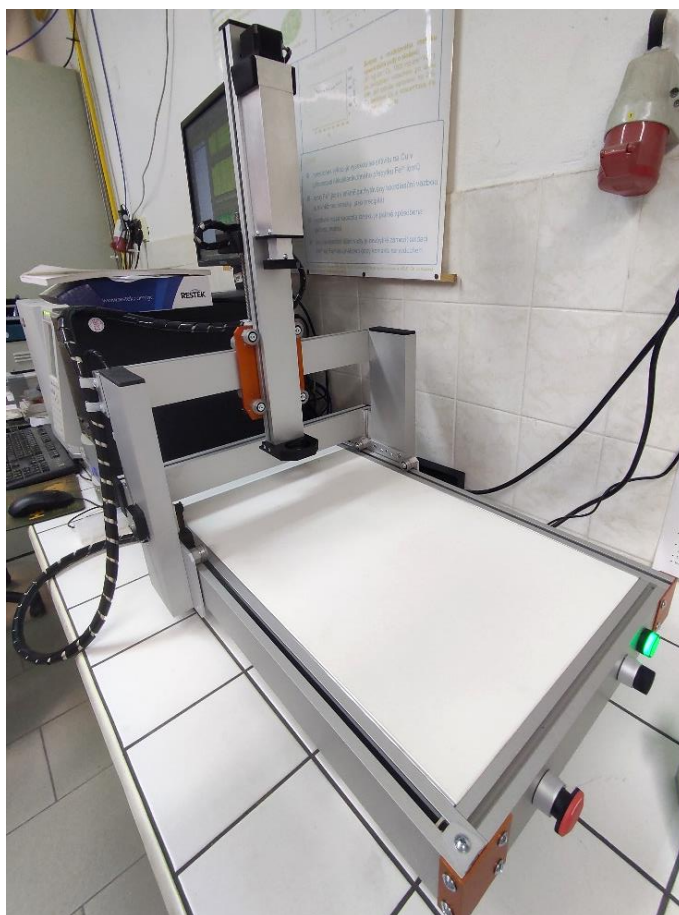


Figure 61 - Tape caster for the automation of the tape casting

5.2.1. Conductivity

Despite the residual porosity presented by the slurry casted electrolyte, its conductivity was successfully measured. The measurement was carried out on a specific sample: the tape was fabricated from a slurry with reference composition and casted at 1000 μm slit height. Then, a 1.5x1.5 cm square was cut from the tape, using a laser. The square was sintered in two steps:

1. Up to 1000 $^{\circ}\text{C}$ it was covered by a thin alumina sheet to prevent any form of bending
2. Reached 1000 $^{\circ}\text{C}$, the sheet was removed and the sample sintered again, following the sintering protocol 1 from the Appendix Table I

After the sintering the Ag electrodes were deposited on the sample and the conductivity was obtained in the same way of the compressed powder-based electrolyte: the ohmic resistance came from the fitting of the EIS spectra and, using Eq. 7, the conductivity was calculated. The thickness of the sample was 0.55 mm (measured with a micrometer) and the electrode area was 2.025 cm² (measured using optical analysis by means of ImageJ freeware analysis software). Only air was considered as gas composition in the furnace. Probably because of the high residual porosity in the sample, the data were recorded correctly only from 550 °C upwards, while the spectra at lower temperatures were not analyzable by means of equivalent circuit fitting and thus had to be discarded.

The EIS spectra are shown in Figure 62. It can be noticed that with increasing temperature the total impedance response decreases and, between two consecutive spectra, this effect becomes more evident as the temperatures result higher. In general, the behavior of the data appeared smooth and well-ordered, with nicely shaped spectra. This can be mainly attributed to the limited range of temperature considered, with the exclusion of the low temperatures from the analysis. For better comprehension, an enlargement of the spectrum at 800 °C is shown in Figure 63.

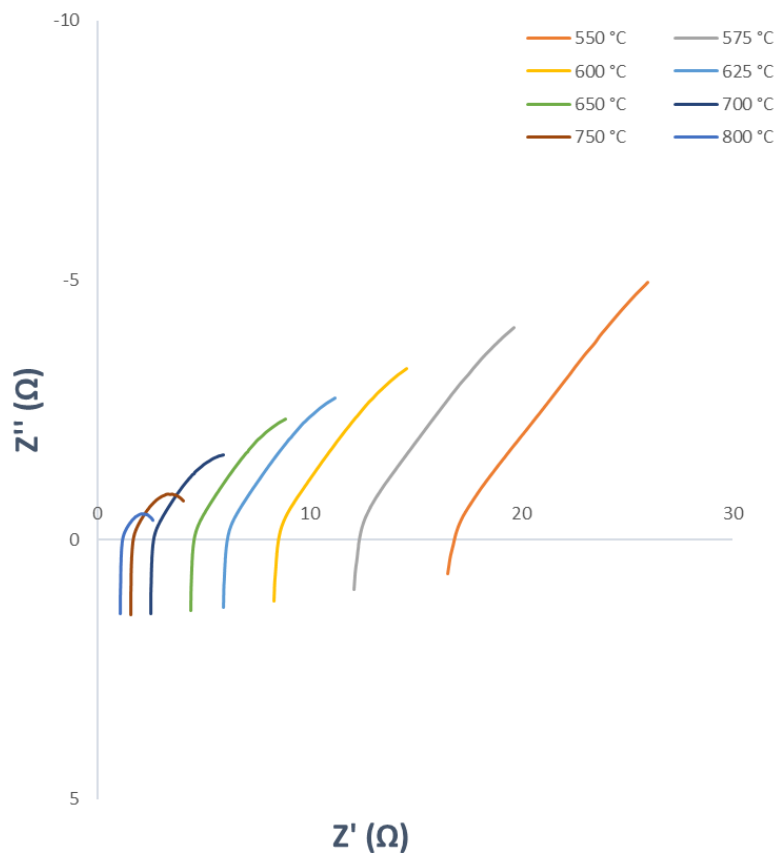


Figure 62 - EIS spectra, slurry casted reference sample, air

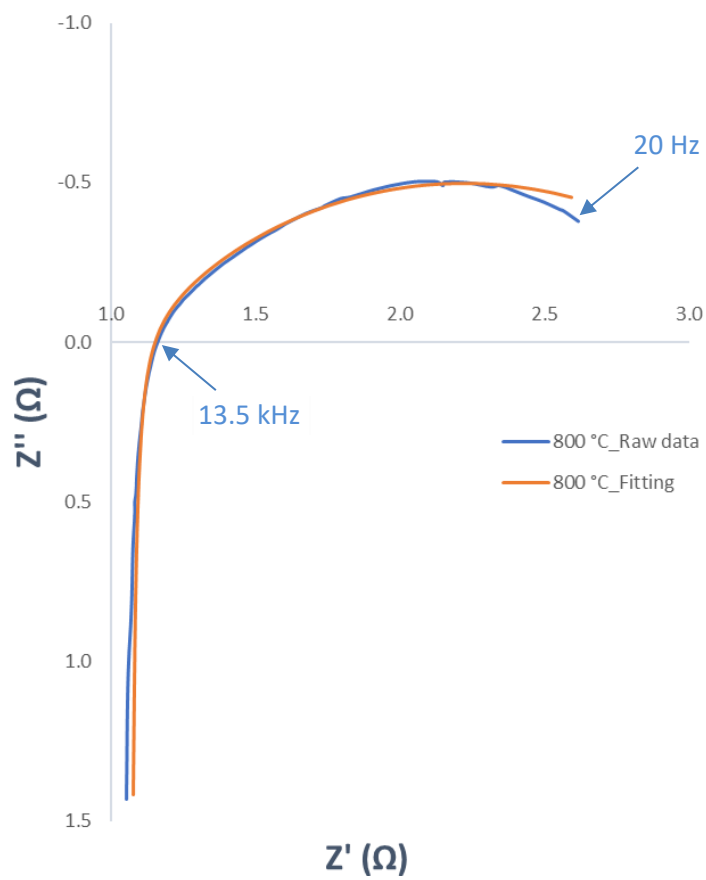


Figure 63 - EIS spectrum, slurry casted reference sample, 800 °C and air

The values of ohmic resistance and conductivity of the electrolyte for each temperature, obtained from the impedance data elaboration, are reported in Table 13.

Temperature [°C]	Ohmic resistance [Ω]	Conductivity [S/m]
550	16.2	0.168
575	11.4	0.237
600	8.02	0.339
625	5.78	0.470
650	4.27	0.636
700	2.49	1.09
750	1.56	1.74
800	1.05	2.59

Table 13 - Ohmic resistance and conductivity of the electrolyte, slurry casted reference sample, air

The obtained results were used to produce the Arrhenius plot in Figure 64. As expected, the conductivity decreases with decreasing temperature and follows the Arrhenius trend.

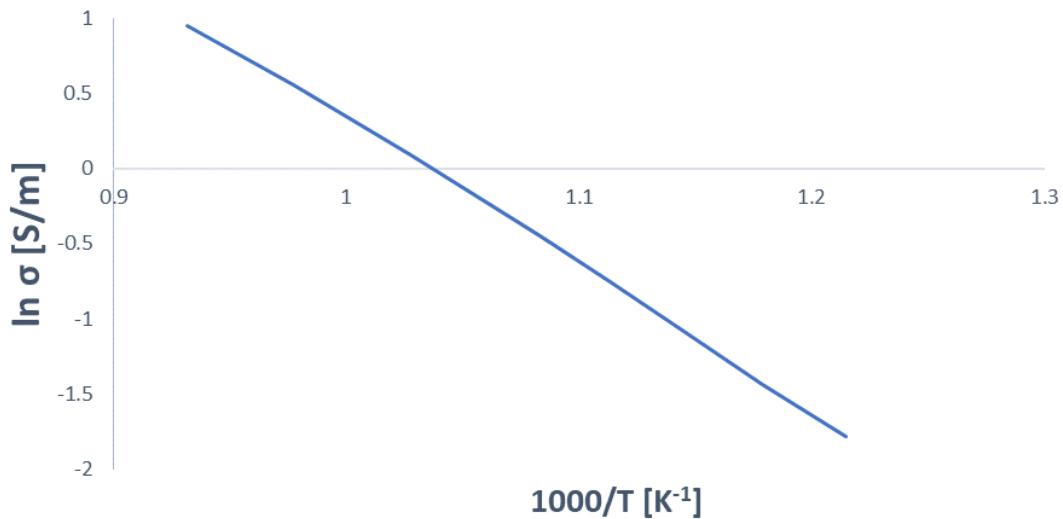


Figure 64 - Arrhenius plot, reference case sample and air

5.3. Comparison of compressed powder-based and slurry casted electrolyte

Both the electrolytes were successfully fabricated. The compressed powder-based electrolyte was thicker (around doubly) than the slurry casted electrolyte. On the other hand, the slurry casted electrolyte resulted highly porous while the compressed-powder based electrolyte was basically tight. The conductivity of both types of electrolyte was measured and compared in Figure 65, where the Arrhenius plots are represented on the same chart. Even though the compressed powder-based electrolyte is thicker, its conductivity is higher. This upshot can be attributed to the high porosity of the slurry casted electrolyte that heavily affects its performances. For this reason, is reasonable to think that, if the porosity problem will be overcome, the slurry casted electrolyte would feature a much higher conductivity.

An aspect in favor of the slurry casting procedure is for sure related to the shape. While with the slurry casting there are ideally no limitations to the geometrical shape and to the size that the electrolyte may have, the powder compression

presents the limitation of the mold that imprints its shape to the green body and, as a consequence, to the electrolyte.

Even though this thesis did not focus on this aspect, the environmental impact of the two procedures has to be taken into account. For sure the slurry casting presents the problem of its not environmentally friendly additives (consider for example to toluene or ethanol) while the powder compression does not need any. A possible solution to make the slurry casting process greener could be that of implementing aqueous solutions for the slurry and, in general, try to switch to more sustainable compounds, considering at the same time that they are more difficult to be managed.

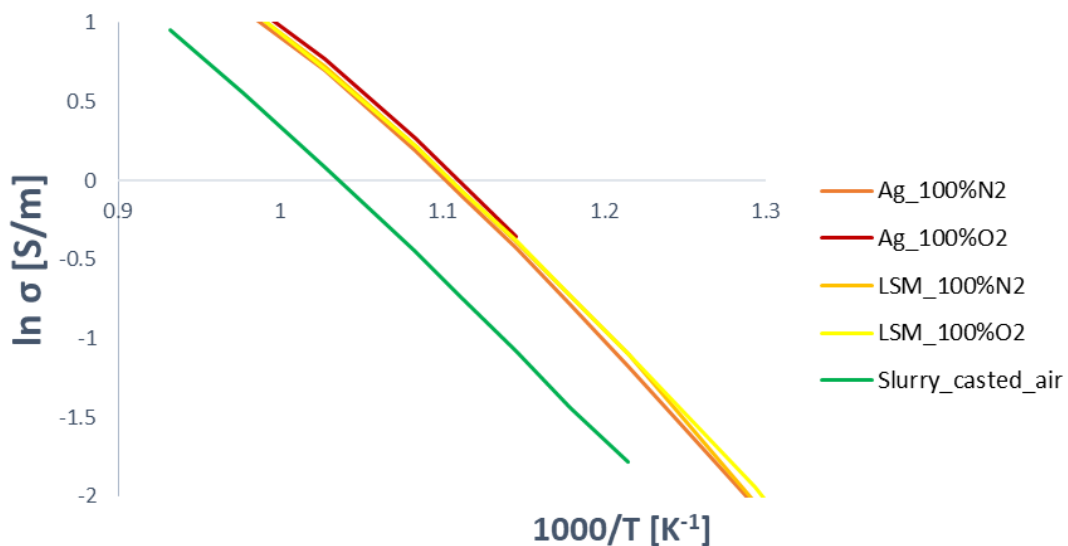


Figure 65 - Arrhenius plots of compressed powder-based and slurry casted electrolyte

6. Conclusions

In this thesis powder compression and slurry casting approach for the fabrication of YSZ electrolytes were investigated. While the former was already optimized, the latter underwent an optimization process. The process did not lead to an ideal solution but left space for further improvements and optimizations. The main merit of this work was, thus, exploring and describing multiple factors influencing the properties of electrolytes fabricated by the tape casting method. To do so, a starting procedure was applied to produce the slurry casted electrolyte. Then, it was gradually modified to see if advantageous differences in the final product would emerge. The modifications interested the slurry composition, the slit height and the sintering temperature and time. The analysis suggested that higher slit height, higher sintering temperature and time and slightly higher amount of YSZ powder and lower amount of PVB binder were beneficial. Also, some additional steps in the fabrication procedure were explored, including the use of chemical solutions and of a void chamber. Despite some defects, the introduction of a solution with YSZ and glycerol seems a promising route.

At the end, the electrolytes were successfully fabricated with both approaches. Their morphology was analyzed by means of optical microscopy and SEM, their composition by means of XRD, their conductivity was measured by means of EIS. The electrochemical characterization of a complete solid oxide cell with compressed powder-based electrolyte was performed employing the EIS and the potentiostatic method.

The compressed powder-based electrolyte resulted in thicker but less porous electrolyte compared to the slurry casted one. Particularly due to the lower

porosity, compressed powder-based electrolyte displayed a higher conductivity. As expected, electrolytes regardless the fabrication method exhibited higher conductivity at higher temperature, with very low value at relatively low temperatures. The electrochemical characterization of the complete cell with compressed powder-based electrolyte shown that the performances of the cell worsen decreasing the operational temperature. Furthermore, the oxygen evolution reaction rate and the oxygen reduction reaction rate result not dependable on the gas atmosphere for all the analyzed temperature levels, but the oxygen reduction reaction rate at 800 °C that is faster at O₂ rich atmosphere. From the environmental point of view, the powder compression does not need any harmful additives as the slurry casting does. Nevertheless, there is the possibility to replace the additives in the slurry with more sustainable and environmentally friendly substances.

7. Bibliography

- [1] "The Future of Hydrogen – Analysis – IEA." Accessed: Feb. 10, 2024. [Online]. Available: <https://www.iea.org/reports/the-future-of-hydrogen>
- [2] "Global Hydrogen Review 2023 – Analysis – IEA." Accessed: Feb. 10, 2024. [Online]. Available: <https://www.iea.org/reports/global-hydrogen-review-2023>
- [3] "World Energy Transitions Outlook 2023: 1.5°C Pathway." Accessed: Feb. 10, 2024. [Online]. Available: <https://www.irena.org/Publications/2023/Jun/World-Energy-Transitions-Outlook-2023>
- [4] A. M. Abdalla, S. Hossain, P. M. I. Petra, M. Ghasemi, and A. K. Azad, "Achievements and trends of solid oxide fuel cells in clean energy field: a perspective review," *Frontiers in Energy*, vol. 14, no. 2. Higher Education Press, pp. 359–382, Jun. 01, 2020. doi: 10.1007/s11708-018-0546-2.
- [5] A. Hagen, H. Langnickel, and X. Sun, "Operation of solid oxide fuel cells with alternative hydrogen carriers," *Int J Hydrogen Energy*, vol. 44, no. 33, pp. 18382–18392, Jul. 2019, doi: 10.1016/j.ijhydene.2019.05.065.
- [6] I. Sreedhar, B. Agarwal, P. Goyal, and S. A. Singh, "Recent advances in material and performance aspects of solid oxide fuel cells," *Journal of Electroanalytical Chemistry*, vol. 848. Elsevier B.V., Sep. 01, 2019. doi: 10.1016/j.jelechem.2019.113315.
- [7] T. M. Gür, "Comprehensive review of methane conversion in solid oxide fuel cells: Prospects for efficient electricity generation from natural gas,"

Progress in Energy and Combustion Science, vol. 54. Elsevier Ltd, pp. 1–64, May 01, 2016. doi: 10.1016/j.pecs.2015.10.004.

- [8] P. Kazempoor and R. J. Braun, "Hydrogen and synthetic fuel production using high temperature solid oxide electrolysis cells (SOECs)," *Int J Hydrogen Energy*, vol. 40, no. 9, pp. 3599–3612, Mar. 2015, doi: 10.1016/j.ijhydene.2014.12.126.
- [9] Q. Fu, C. Mabilat, M. Zahid, A. Brisse, and L. Gautier, "Syngas production via high-temperature steam/CO₂ co-electrolysis: An economic assessment," *Energy Environ Sci*, vol. 3, no. 10, pp. 1382–1397, Oct. 2010, doi: 10.1039/c0ee00092b.
- [10] H. Yokokawa, T. Horita, K. Yamaji, H. Kishimoto, and M. E. Brito, "Degradation of SOFC cell/stack performance in relation to materials deterioration," *Journal of the Korean Ceramic Society*, vol. 49, no. 1. pp. 11–18, Jan. 2012. doi: 10.4191/kcers.2012.49.1.011.
- [11] P. Moçoteguy and A. Brisse, "A review and comprehensive analysis of degradation mechanisms of solid oxide electrolysis cells," *International Journal of Hydrogen Energy*, vol. 38, no. 36. pp. 15887–15902, Dec. 13, 2013. doi: 10.1016/j.ijhydene.2013.09.045.
- [12] K. Chen and S. P. Jiang, "Review—Materials Degradation of Solid Oxide Electrolysis Cells," *J Electrochem Soc*, vol. 163, no. 11, pp. F3070–F3083, 2016, doi: 10.1149/2.010161jes.
- [13] M. S. Khan, X. Xu, R. Knibbe, and Z. Zhu, "Air electrodes and related degradation mechanisms in solid oxide electrolysis and reversible solid oxide cells," *Renewable and Sustainable Energy Reviews*, vol. 143. Elsevier Ltd, Jun. 01, 2021. doi: 10.1016/j.rser.2021.110918.

- [14] P. Kazempoor and R. J. Braun, "Model validation and performance analysis of regenerative solid oxide cells: Electrolytic operation," *Int J Hydrogen Energy*, vol. 39, no. 6, pp. 2669–2684, Feb. 2014, doi: 10.1016/j.ijhydene.2013.12.010.
- [15] N. A. Baharuddin, A. Muchtar, A. B. Sulong, and H. Abdullah, "Fabrication methods for planar solid oxide fuel cells: A review," in *Advanced Materials Research*, 2013, pp. 396–401. doi: 10.4028/www.scientific.net/AMR.662.396.
- [16] P. Singh and N. Q. Minh, "Ceramic Product Development and Commercialization Solid Oxide Fuel Cells: Technology Status," *Int. J. Appl. Ceram. Technol*, vol. 1, no. 1, pp. 5–15, 2004, [Online]. Available: www.ceramics.org/ACT
- [17] R. N. Singh, "Sealing Technology for Solid Oxide Fuel Cells (SOFC)," *Int J Appl Ceram Technol*, vol. 4, no. 2, pp. 134–144, Mar. 2007, doi: 10.1111/J.1744-7402.2007.02128.X.
- [18] G. Li, Y. Gou, J. Qiao, W. Sun, Z. Wang, and K. Sun, "Recent progress of tubular solid oxide fuel cell: From materials to applications," *J Power Sources*, vol. 477, Nov. 2020, doi: 10.1016/j.jpowsour.2020.228693.
- [19] B. Timurkutluk, C. Timurkutluk, M. D. Mat, and Y. Kaplan, "A review on cell/stack designs for high performance solid oxide fuel cells," *Renewable and Sustainable Energy Reviews*, vol. 56. Elsevier Ltd, pp. 1101–1121, Apr. 01, 2016. doi: 10.1016/j.rser.2015.12.034.
- [20] M. Irshad *et al.*, "A brief description of high temperature solid oxide fuel cell's operation, materials, design, fabrication technologies and performance," *Applied Sciences (Switzerland)*, vol. 6, no. 3. MDPI AG, 2016. doi: 10.3390/app6030075.

- [21] D. Udomsilp, C. Lenser, O. Guillon, and N. H. Menzler, "Performance Benchmark of Planar Solid Oxide Cells Based on Material Development and Designs," *Energy Technology*, vol. 9, no. 4. John Wiley and Sons Inc, Apr. 01, 2021. doi: 10.1002/ente.202001062.
- [22] A. Nechache and S. Hody, "Alternative and innovative solid oxide electrolysis cell materials: A short review," *Renewable and Sustainable Energy Reviews*, vol. 149. Elsevier Ltd, Oct. 01, 2021. doi: 10.1016/j.rser.2021.111322.
- [23] S. Dwivedi, "Solid oxide fuel cell: Materials for anode, cathode and electrolyte," *Int J Hydrogen Energy*, vol. 45, no. 44, pp. 23988–24013, Sep. 2020, doi: 10.1016/j.ijhydene.2019.11.234.
- [24] S. Hussain and L. Yangping, "Review of solid oxide fuel cell materials: cathode, anode, and electrolyte," *Energy Transitions*, vol. 4, no. 2, pp. 113–126, Dec. 2020, doi: 10.1007/s41825-020-00029-8.
- [25] N. Laosiripojana, W. Wiyaratn, W. Kiatkittipong, A. Arpornwichanop, A. Soottitantawat, and S. Assabumrungrat, "Reviews on solid oxide fuel cell technology," *Engineering Journal*, vol. 13, no. 1, pp. 65–83, 2009, doi: 10.4186/ej.2009.13.1.65.
- [26] F. S. da Silva and T. M. de Souza, "Novel materials for solid oxide fuel cell technologies: A literature review," *International Journal of Hydrogen Energy*, vol. 42, no. 41. Elsevier Ltd, pp. 26020–26036, Oct. 12, 2017. doi: 10.1016/j.ijhydene.2017.08.105.
- [27] S. A. M. Ali, R. E. Rosli, A. Muchtar, A. B. Sulong, M. R. Somalu, and E. H. Majlan, "Effect of sintering temperature on surface morphology and electrical properties of samarium-doped ceria carbonate for solid oxide fuel cells,"

Ceram Int, vol. 41, no. 1, pp. 1323–1332, 2015, doi:

10.1016/j.ceramint.2014.09.064.

- [28] A. Weber and E. Ivers-Tiffée, “Materials and concepts for solid oxide fuel cells (SOFCs) in stationary and mobile applications,” in *Journal of Power Sources*, Mar. 2004, pp. 273–283. doi: 10.1016/j.jpowsour.2003.09.024.
- [29] M. B. Mogensen, “Materials for reversible solid oxide cells,” *Current Opinion in Electrochemistry*, vol. 21. Elsevier B.V., pp. 265–273, Jun. 01, 2020. doi: 10.1016/j.coelec.2020.03.014.
- [30] S. Tao and J. T. S. Irvine, “Discovery and characterization of novel oxide anodes for solid oxide fuel cells,” *Chemical Record*, vol. 4, no. 2. pp. 83–95, 2004. doi: 10.1002/tcr.20003.
- [31] J. W. Fergus, “Oxide anode materials for solid oxide fuel cells,” *Solid State Ion*, vol. 177, no. 17–18, pp. 1529–1541, Jul. 2006, doi: 10.1016/j.ssi.2006.07.012.
- [32] Y. Chen *et al.*, “Advances in Cathode Materials for Solid Oxide Fuel Cells: Complex Oxides without Alkaline Earth Metal Elements,” *Adv Energy Mater*, vol. 5, no. 18, Sep. 2015, doi: 10.1002/aenm.201500537.
- [33] M. Carda, N. Adamová, D. Budáč, V. Rečková, M. Paidar, and K. Bouzek, “Impact of Preparation Method and Y₂O₃ Content on the Properties of the YSZ Electrolyte,” *Energies (Basel)*, vol. 15, no. 7, Apr. 2022, doi: 10.3390/en15072565.
- [34] X. Xin *et al.*, “Solid oxide fuel cells with dense yttria-stabilized zirconia electrolyte membranes fabricated by a dry pressing process,” *J Power Sources*, vol. 160, no. 2 SPEC. ISS., pp. 1221–1224, Oct. 2006, doi: 10.1016/j.jpowsour.2006.02.073.
- [35] H. Chang *et al.*, “Preparation of thin electrolyte film via dry pressing/heating /quenching/calcining for electrolyte-supported SOFCs,”

Ceram Int, vol. 45, no. 8, pp. 9866–9870, Jun. 2019, doi:
10.1016/j.ceramint.2019.02.026.

- [36] D. Hotza and P. Greil, "A Review: aqueous tape casting of ceramic powders," *Materials Science and Engineering: A*, vol. 202, no. 1–2, pp. 206–217, 1995.
- [37] A. S. Deepi, S. Dharani Priya, A. Samson Nesaraj, and A. I. Selvakumar, "Component fabrication techniques for solid oxide fuel cell (SOFC)–A comprehensive review and future prospects," *International Journal of Green Energy*, vol. 19, no. 14. Taylor and Francis Ltd., pp. 1600–1612, 2022. doi: 10.1080/15435075.2021.2018320.
- [38] Z. Shen, X. Zhu, S. Le, W. Sun, and K. Sun, "Co-sintering anode and Y2O3 stabilized ZrO₂ thin electrolyte film for solid oxide fuel cell fabricated by co-tape casting," *Int J Hydrogen Energy*, vol. 37, no. 13, pp. 10337–10345, 2012, doi: 10.1016/j.ijhydene.2012.04.022.
- [39] S. Ramanathan and M. B. Kakade, "Aqueous slurry processing of monolithic films for SOFC – YSZ, LSM and YSZ–NiO systems," *Int J Hydrogen Energy*, vol. 36, no. 22, pp. 14956–14962, Nov. 2011, doi: 10.1016/j.ijhydene.2011.06.112.
- [40] J. Zhou, Q. Liu, Q. Sun, and S. Hwa Chan, "A low cost large-area solid oxide cells fabrication technology based on aqueous Co-tape casting and Co-sintering," *Fuel Cells*, vol. 14, no. 4, pp. 667–670, Aug. 2014, doi: 10.1002/fuce.201300212.
- [41] S. Lee, K. Lee, Y. hoon Jang, and J. Bae, "Fabrication of solid oxide fuel cells (SOFCs) by solvent-controlled co-tape casting technique," *Int J Hydrogen Energy*, vol. 42, no. 3, pp. 1648–1660, Jan. 2017, doi: 10.1016/j.ijhydene.2016.07.066.

- [42] P. Timakul, S. Jinawath, and P. Aungkavattana, "Fabrication of electrolyte materials for solid oxide fuel cells by tape-casting," *Ceram Int*, vol. 34, no. 4, pp. 867–871, May 2008, doi: 10.1016/j.ceramint.2007.09.038.
- [43] M. Jabbari, R. Bulatova, A. I. Y. Tok, C. R. H. Bahl, E. Mitsoulis, and J. H. Hattel, "Ceramic tape casting: A review of current methods and trends with emphasis on rheological behaviour and flow analysis," *Materials Science and Engineering: B*, vol. 212. Elsevier Ltd, pp. 39–61, Oct. 01, 2016. doi: 10.1016/j.mseb.2016.07.011.
- [44] M. Han, X. Tang, H. Yin, and S. Peng, "Fabrication, microstructure and properties of a YSZ electrolyte for SOFCs," *J Power Sources*, vol. 165, no. 2, pp. 757–763, Mar. 2007, doi: 10.1016/j.jpowsour.2006.11.054.
- [45] T. Talebi, M. Haji, and B. Raissi, "Effect of sintering temperature on the microstructure, roughness and electrochemical impedance of electrophoretically deposited YSZ electrolyte for SOFCs," in *International Journal of Hydrogen Energy*, Sep. 2010, pp. 9420–9426. doi: 10.1016/j.ijhydene.2010.05.079.
- [46] A. J. Bard, L. R. Faulkner, and H. S. White, *Electrochemical methods: fundamentals and applications*, Third edition. 2022.
- [47] A. Nechache, M. Cassir, and A. Ringuedé, "Solid oxide electrolysis cell analysis by means of electrochemical impedance spectroscopy: A review," *Journal of Power Sources*, vol. 258. pp. 164–181, Jul. 15, 2014. doi: 10.1016/j.jpowsour.2014.01.110.
- [48] P. Hofmann and K. D. Panopoulos, "Detailed dynamic Solid Oxide Fuel Cell modeling for electrochemical impedance spectra simulation," *J Power Sources*, vol. 195, no. 16, pp. 5320–5339, Aug. 2010, doi: 10.1016/j.jpowsour.2010.02.046.

- [49] N. Wagner, W. Schnurnberger, M. Lang, and B. Muller, "Electrochemical impedance spectra of solid-oxide fuel cells and polymer membrane fuel cells," *Electrochimica Acta*, vol. 43, no. 24, pp. 3785–3793, 1998.
- [50] M. Carda, D. Budáč, M. Paidar, and K. Bouzek, "Current trends in the description of lanthanum strontium manganite oxygen electrode reaction mechanism in a high-temperature solid oxide cell," *Current Opinion in Electrochemistry*, vol. 31. Elsevier B.V., Feb. 01, 2022. doi: 10.1016/j.coelec.2021.100852.

8. Appendix

– Sintering protocols

Protocol number	Purpose	Step number												
		1	2	3	4	5	6	7	8	9	10	11	12	13
1	1360 °C sintering	r1.3	t900	r1.1	t1100	d60	r1.1	t1360	d360	r1.2	t180			
2	1550 °C sintering	r1.3	t900	r1.1	t1100	d60	r1.1	t1360	d360	r1.0	t1550	d1440	r1.2	t180
3	Ag electrodes	r1.0	t100	d120	r1.5	t800	d120	t1.5	t100					
4	LSM electrodes	r1.8	t1150	d180	r1.8	t100								

Appendix Table I – Sintering protocols

Here r is a temperature ramp between current and following temperature in °C/min, t is a temperature in °C, d is a delay on a current temperature in min. The bold text signifies the sintering temperature and its corresponding duration. After the furnace reached the last set temperature it was turned off and subsequent cooling was free of any control.

– Electrochemical characterization of the compressed powder based electrolyte cell

Voltage	Overpotential	Current	Current density	R	R _{corr}	OCP	Area
0.014	0	0	0	0.405	0.365	0.014	2.01
0.1	0.062	0.064	0.032	0.393	0.353		
0.2	0.125	0.171	0.085	0.390	0.351		
0.3	0.160	0.364	0.181	0.381	0.344		
0.4	0.185	0.604	0.300	0.368	0.332		
0.5	0.199	0.897	0.446	0.354	0.319		
0.6	0.209	1.22	0.608	0.341	0.307		
0.7	0.215	1.57	0.784	0.331	0.298		

0.6	0.191	1.20	0.598	0.363	0.327
0.5	0.169	0.894	0.444	0.393	0.354
0.4	0.148	0.631	0.314	0.418	0.376
0.3	0.124	0.414	0.206	0.432	0.389
0.2	0.095	0.229	0.114	0.434	0.391
0.1	0.055	0.080	0.039	0.423	0.382
-0.1	-0.062	-0.130	-0.065	0.436	0.393
-0.2	-0.113	-0.248	-0.123	0.451	0.406
-0.3	-0.151	-0.398	-0.198	0.453	0.408
-0.4	-0.184	-0.571	-0.284	0.447	0.402
-0.5	-0.209	-0.770	-0.383	0.440	0.396
-0.6	-0.232	-0.998	-0.496	0.424	0.382
-0.7	-0.257	-1.26	-0.628	0.401	0.361
-0.6	-0.214	-1.09	-0.543	0.406	0.366
-0.5	-0.178	-0.904	-0.449	0.412	0.371
-0.4	-0.147	-0.721	-0.358	0.411	0.370
-0.3	-0.112	-0.542	-0.269	0.412	0.371
-0.2	-0.077	-0.368	-0.183	0.413	0.372
-0.1	-0.041	-0.197	-0.098	0.410	0.369

Appendix Table II - Results of electrochemical characterization, compressed powder, 800 °C and 100% O₂

Voltage	Overpotential	Current	Current density	R	R _{corr}	OCP	Area
-0.010	0	0	0	0.428	0.386	-0.010	2.01
0.1	0.068	0.103	0.051	0.439	0.395		
0.2	0.131	0.187	0.093	0.462	0.416		
0.3	0.164	0.352	0.175	0.456	0.411		
0.4	0.184	0.559	0.278	0.448	0.403		
0.5	0.196	0.806	0.401	0.432	0.389		
0.6	0.204	1.08	0.541	0.414	0.372		
0.7	0.210	1.41	0.703	0.392	0.352		
0.6	0.191	1.10	0.549	0.420	0.378		
0.5	0.175	0.834	0.415	0.445	0.400		
0.4	0.158	0.603	0.300	0.463	0.417		
0.3	0.136	0.407	0.202	0.473	0.426		

0.2	0.107	0.235	0.117	0.483	0.435
0.1	0.066	0.100	0.050	0.485	0.436
-0.1	-0.053	-0.084	-0.042	0.480	0.432
-0.2	-0.112	-0.177	-0.088	0.485	0.437
-0.3	-0.163	-0.284	-0.141	0.492	0.443
-0.4	-0.211	-0.405	-0.201	0.487	0.438
-0.5	-0.252	-0.547	-0.272	0.482	0.433
-0.6	-0.292	-0.712	-0.354	0.463	0.417
-0.7	-0.337	-0.898	-0.447	0.435	0.391
-0.6	-0.272	-0.785	-0.390	0.449	0.404
-0.5	-0.224	-0.654	-0.325	0.450	0.405
-0.4	-0.179	-0.523	-0.260	0.447	0.402
-0.3	-0.131	-0.393	-0.195	0.446	0.402
-0.2	-0.086	-0.263	-0.131	0.438	0.394
-0.1	-0.039	-0.129	-0.064	0.429	0.386

Appendix Table III - Results of electrochemical characterization, compressed powder, 800 °C and 20% O₂

Voltage	Overpotential	Current	Current density	R	R _{corr}	OCP	Area
0.012	0	0	0	1.03	0.931	0.012	2.01
0.1	0.032	0.049	0.024	1.13	1.01		
0.2	0.097	0.080	0.039	1.12	1.01		
0.3	0.128	0.140	0.070	1.13	1.01		
0.4	0.144	0.219	0.109	1.10	0.998		
0.5	0.155	0.308	0.153	1.07	0.969		
0.6	0.163	0.406	0.201	1.04	0.942		
0.7	0.168	0.513	0.255	1.01	0.910		
0.6	0.157	0.406	0.202	1.06	0.954		
0.5	0.147	0.308	0.153	1.10	0.996		
0.4	0.134	0.220	0.109	1.14	1.03		
0.3	0.119	0.143	0.071	1.17	1.05		
0.2	0.090	0.084	0.041	1.16	1.04		
0.1	0.042	0.039	0.019	1.15	1.04		
-0.1	-0.045	-0.058	-0.029	1.12	1.01		
-0.2	-0.069	-0.125	-0.062	1.13	1.02		

-0.3	-0.091	-0.195	-0.097	1.12	1.0107
-0.4	-0.115	-0.269	-0.134	1.10	0.990
-0.5	-0.134	-0.348	-0.173	1.08	0.974
-0.6	-0.161	-0.434	-0.216	1.03	0.933
-0.7	-0.171	-0.529	-0.263	1.02	0.918
-0.6	-0.149	-0.452	-0.225	1.02	0.919
-0.5	-0.130	-0.372	-0.185	1.02	0.919
-0.4	-0.105	-0.295	-0.146	1.03	0.935
-0.3	-0.085	-0.219	-0.108	1.03	0.929
-0.2	-0.062	-0.144	-0.072	1.03	0.927
-0.1	-0.036	-0.073	-0.036	1.02	0.926

Appendix Table IV - Results of electrochemical characterization, compressed powder, 700 °C and 100% O₂

Voltage	Overpotential	Current	Current density	R	R _{corr}	OCP	Area
0.012	0	0	0	1.02	0.920	0.012	2.01
0.1	0.036	0.049	0.024	1.17	1.05		
0.2	0.100	0.085	0.042	1.14	1.03		
0.3	0.144	0.138	0.069	1.15	1.03		
0.4	0.166	0.216	0.107	1.13	1.02		
0.5	0.184	0.304	0.151	1.10	0.998		
0.6	0.201	0.400	0.199	1.07	0.965		
0.7	0.214	0.507	0.252	1.03	0.935		
0.6	0.197	0.402	0.200	1.07	0.971		
0.5	0.177	0.306	0.152	1.12	1.01		
0.4	0.158	0.219	0.109	1.16	1.04		
0.3	0.134	0.144	0.071	1.18	1.06		
0.2	0.097	0.085	0.042	1.17	1.05		
0.1	0.045	0.040	0.020	1.18	1.06		
-0.1	-0.051	-0.061	-0.030	1.09	0.987		
-0.2	-0.084	-0.127	-0.063	1.11	1.00		
-0.3	-0.113	-0.197	-0.098	1.11	1.00		
-0.4	-0.145	-0.272	-0.135	1.08	0.977		
-0.5	-0.173	-0.350	-0.174	1.07	0.964		
-0.6	-0.204	-0.437	-0.217	1.03	0.932		

-0.7	-0.235	-0.532	-0.264	0.995	0.895
-0.6	-0.198	-0.454	-0.225	1.01	0.909
-0.5	-0.163	-0.373	-0.185	1.03	0.930
-0.4	-0.141	-0.295	-0.147	1.01	0.912
-0.3	-0.110	-0.219	-0.109	1.01	0.916
-0.2	-0.077	-0.144	-0.072	1.02	0.926
-0.1	-0.044	-0.073	-0.036	1.01	0.916

Appendix Table V - Results of electrochemical characterization, compressed powder, 700 °C and 20% O₂

Voltage	Overpotential	Current	Current density	R	R _{corr}	OCP	Area
0.010	0	0	0	3.58	3.22	0.010	2.01
0.1	0.036	0.016	0.008	3.68	3.31		
0.2	0.100	0.027	0.013	3.64	3.28		
0.3	0.143	0.044	0.022	3.66	3.29		
0.4	0.166	0.068	0.034	3.62	3.26		
0.5	0.184	0.094	0.047	3.57	3.22		
0.6	0.198	0.123	0.061	3.51	3.16		
0.7	0.208	0.154	0.077	3.45	3.10		
0.6	0.199	0.122	0.060	3.55	3.19		
0.5	0.187	0.092	0.045	3.63	3.27		
0.4	0.170	0.065	0.032	3.72	3.35		
0.3	0.148	0.041	0.020	3.80	3.42		
0.2	0.112	0.022	0.011	3.78	3.40		
0.1	0.050	0.011	0.005	3.84	3.46		
-0.1	-0.054	-0.017	-0.008	3.58	3.22		
-0.2	-0.093	-0.035	-0.017	3.64	3.27		
-0.3	-0.126	-0.056	-0.027	3.62	3.26		
-0.4	-0.159	-0.077	-0.038	3.59	3.23		
-0.5	-0.187	-0.100	-0.049	3.58	3.22		
-0.6	-0.214	-0.122	-0.061	3.57	3.21		
-0.7	-0.250	-0.146	-0.072	3.48	3.13		
-0.6	-0.212	-0.125	-0.062	3.52	3.17		

-0.5	-0.181	-0.103	-0.051	3.52	3.16
-0.4	-0.149	-0.082	-0.040	3.51	3.16
-0.3	-0.116	-0.061	-0.030	3.49	3.14
-0.2	-0.082	-0.040	-0.020	3.50	3.15
-0.1	-0.046	-0.020	-0.010	3.50	3.15

Appendix Table VI – Results of electrochemical characterization, compressed powder, 600 °C and 100% O₂

Voltage	Overpotential	Current	Current density	R	R _{corr}	OCP	Area
0.010	0	0	0	3.59	3.23	0.010	2.01
0.1	0.034	0.016	0.008	3.84	3.45		
0.2	0.088	0.029	0.014	3.84	3.45		
0.3	0.138	0.044	0.021	3.82	3.44		
0.4	0.166	0.066	0.033	3.73	3.36		
0.5	0.188	0.091	0.045	3.66	3.30		
0.6	0.205	0.118	0.059	3.59	3.23		
0.7	0.218	0.148	0.073	3.53	3.17		
0.6	0.206	0.117	0.058	3.62	3.25		
0.5	0.191	0.089	0.044	3.70	3.33		
0.4	0.172	0.063	0.031	3.78	3.40		
0.3	0.146	0.040	0.020	3.91	3.52		
0.2	0.109	0.023	0.011	3.89	3.50		
0.1	0.049	0.011	0.005	3.90	3.51		
-0.1	-0.050	-0.018	-0.008	3.63	3.26		
-0.2	-0.092	-0.035	-0.017	3.64	3.27		
-0.3	-0.127	-0.056	-0.027	3.61	3.24		
-0.4	-0.160	-0.077	-0.038	3.58	3.22		
-0.5	-0.190	-0.099	-0.049	3.58	3.22		
-0.6	-0.219	-0.121	-0.060	3.56	3.21		
-0.7	-0.245	-0.144	-0.072	3.56	3.20		
-0.6	-0.214	-0.123	-0.061	3.54	3.19		
-0.5	-0.184	-0.102	-0.050	3.53	3.17		
-0.4	-0.149	-0.081	-0.040	3.54	3.19		
-0.3	-0.118	-0.060	-0.030	3.51	3.15		
-0.2	-0.083	-0.039	-0.019	3.51	3.16		

-0.1	-0.046	-0.019	-0.009	3.52	3.16
------	--------	--------	--------	------	------

Appendix Table VII – Results of electrochemical characterization, compressed powder, 600 °C and 20% O₂